Ore Geology Reviews 76 (2015) 442–462

Contents lists available at ScienceDirect

Ore Geology Reviews

journal homepage: www.elsevier.com/locate/oregeorev

The Mesoproterozoic Abra polymetallic sedimentary rock-hosted mineral deposit, Edmund Basin, Western Australia

Franco Pirajno [a,*], Terrence P. Mernagh [b], David Huston [b], Robert A. Creaser [c], Reimar Seltmann [d]

[a] Centre for Exploration Targeting, University of Western Australia, 35 Stirling Highway, Crawley WA6009, Australia
[b] Geoscience Australia, GPO Box 378, Canberra, ACT 2601, Australia
[c] Dept Earth & Atmospheric Sciences, University of Alberta, 126 Earth Sciences Building, Edmonton, AB T6G 2R3, Canada
[d] Centre for Russian and Central EurAsian Mineral Studies (CERCAMS), Department of Earth Sciences, Natural History Museum, Cromwell Road, London SW7 5BD, UK

ARTICLE INFO

Article history:
Received 27 November 2014
Received in revised form 17 April 2015
Accepted 23 April 2015
Available online 26 April 2015

Keywords:
Edmund Basin
Abra deposit
Fluid inclusions
Sulphur and lead isotopes
Re–Os dating
SEDEX model
Seismic enhanced multi-phase fluids

ABSTRACT

Abra is a blind, sedimentary rock-hosted polymetallic Fe–Pb–Zn–Ba–Cu ± Au ± Ag ± Bi ± W deposit, discovered in 1981, located within the easterly trending Jillawarra rift sub-basin of the Mesoproterozoic Edmund Basin, Capricorn Orogen, Western Australia. The Edmund Basin contains a 4–10 km thick succession of siltstone, sandstone, dolomitic siltstone, and stromatolitic dolomite. The age of the Edmund Group is between 1.66 and 1.46 Ga. The Abra polymetallic deposit is hosted in siltstone, dolostone, sandstone and conglomerate of the Irregully and Kiangi Creek Formations, but the mineralised zones do not extend above an erosion surface marking the change from fluvial to marine facies in the lower part of the Kiangi Creek Formation. The Abra deposit is characterised by a funnel-shaped brecciated zone, interpreted as a feeder pipe, overlain by stratiform–stratabound mineralisation. The stratiform–stratabound mineralisation includes a Red Zone and an underlying Black Zone. The Red Zone is characterised by banded jaspilite, hematite, galena, pyrite, quartz, barite, and siderite. The jaspilite and hematite cause the predominant red colouration. The Black Zone consists of veins and rhythmically banded sulphides, laminated and/or brecciated hematite, magnetite, Fe-rich carbonate and scheelite. In both zones, laminations and bands of sulphide minerals, Fe oxides, barite and quartz commonly exhibit colloform textures. The feeder pipe (Stringer Zone) merges with Black Zone and consists of a stockwork of Fe-carbonate-quartz, barite, pyrite, magnetite and chalcopyrite, exhibiting fluidised and/or jigsaw textures.

The Abra mineral system is characterised by several overprinting phases of hydrothermal activity, from several stages of brecciation and fluidisation, barite and sulphide veining to barren low-temperature chalcedonic (epithermal regime) veining. Hydrothermal alteration minerals include multi-stage quartz, chlorite, prehnite, Fe-rich carbonate and albite. Albite (Na metasomatism) is an early alteration phase, whereas Fe-rich carbonate is a late phase. Fluid inclusion studies indicate that the ore fluids had temperatures ranging from 162 to 250 °C, with salinities ranging from 5.8 to about 20 wt.% NaCl. In the course of our studies, microthermometric and Raman microprobe analyses were performed on fluid inclusions in carbonate, quartz and barite grains. Fluid inclusions in quartz show homogenisation temperatures ranging from 150 to 170 °C with calculated salinities of between 3.7 and 13.8 wt.% NaCl.

The sulphur isotopic system shows $\delta^{34}S$ values ranging from 19.4 to 26.6‰ for sulphides and from 37.4 to 41.9‰ for barite (Vogt and Stumpfl, 1987; Austen, 2007). Sulphur isotope thermometry between sulphides and sulphide–barite pairs yields values ranging from 219 to 336 °C (Austen, 2007).

Galena samples were analysed for Pb isotope ratios, which have been compared with previous Pb isotopic data. The new Pb isotope systematics show model ages of 1650–1628 Ma, consistent with the formation of the host Edmund Basin.

Re–Os dating of euhedral pyrite from the Black Zone yielded an age of ~1255 Ma. This age corresponds to the 1320–1170 Ma Mutherbukin tectonic event in the Gascoyne Complex. This event is manifested primarily along a WNW-trending structural corridor of amphibolite facies rocks, about 250 km to the northwest of the Abra area. It is possible that the Re–Os age represents a younger re-activation event of an earlier SEDEX style system with a possible age range of 1640–1590 Ma.

A genetic model for Abra is proposed based on the above data. The model involves two end-members ore-forming stages: the first is the formation of the SEDEX style mineral systems, followed by a second multi-

* Corresponding author.
E-mail address: franco.pirajno@uwa.edu.au (F. Pirajno).

http://dx.doi.org/10.1016/j.oregeorev.2015.04.019
0169-1368/© 2015 Elsevier B.V. All rights reserved.

phase stage during which there was repeated re-working of the mineral system, guided by seismic activity along major regional faults.

© 2015 Elsevier B.V. All rights reserved.

1. Introduction

Abra is a blind, sedimentary rock-hosted polymetallic Fe–Pb–Zn–Ba–Cu ± Au ± Ag ± Bi ± W deposit, discovered in 1981, located within the easterly trending Jillawarra rift sub-basin of the Mesoproterozoic Edmund Basin. The Edmund Basin contains a 4–10 km thick succession of siltstone, sandstone, dolomitic siltstone, and stromatolitic dolomite. The age of the Edmund Group is between 1.66 and 1.46 Ga (Martin and Thorne, 2004). Igneous activity in the Jillawarra sub-basin includes high-K rhyolite (Tangadee Rhyolite), with a poorly constrained U–Pb zircon age of 1.64 Ga (Nelson, 1995) and a xenotime age of 1.23 Ga (Rasmussen et al., 2010). In addition, the Edmund Group is intruded by voluminous ~1465 Ma and ~1070 Ma mafic sills, which caused local inflation of the stratigraphic thickness of up to 60% (Morris and Pirajno, 2005 and references therein).

The Abra mineralisation was first described by Vogt and Stumpfl (1987), Boddington (1990), Collins and McDonald (1994), Vogt (1995) and Cooper et al. (1998). Austen (2007) carried out a petrographic, fluid inclusion and isotope systematics study of the Abra deposit. Later investigations include Pirajno et al. (2010), Rasmussen et al. (2010) and Zi et al. (2015). Fig. 1, shows the position of the Abra area in the Bangemall Basin and the Jillawara rift or sub-basin. Cooper et al. (1998), reported that in the western part of the Jillawara rift there are other base metal and Fe occurrences, such as those at Woodlands and Gnamma, which are located in a large (6 km in diameter) magnetic anomaly (Fig. 2). It is of interest to note that in this anomaly a drillhole intersected barite, magnetite and siderite veins in dolomitic carbonate rocks. Cooper et al. (1998) suggested the possibility of a carbonatitic system for these occurrences.

The Abra deposit is still in an exploration stage and is estimated to contain approximately 93 Mt, grading 4% Pb,10 g/t Ag and a stockwork zone enriched in gold with 14 Mt at 0.62% Cu and 0.5 g/t Au (http://www.abramining.com.au/ November 2008 and Abra Mining Ltd; see Table 1 for details). The Abra mineralisation lies beneath a 200 to 350 m cover of the Kiangi Creek Formation (Edmund Group; Martin and Thorne, 2004; Cutten et al., in press), and therefore all observations and features herein described are the result of the study of drill core. Selected drilling results indicate that Abra is a large, but generally low-grade deposit, with some of the best intersections yielding 58 m at 9.7% Pb and 4.5 g/t Ag; 12.8 m at 9.5% Pb, 15.5 g/t Ag and 2.8% Zn; 56 m at 3.4% Pb, 15 g/t Ag and 0.3 g/t Au (Media release to the Australian Stock Exchange, January 2008). In addition, drilling programmes have revealed the presence of a cluster of similar prospects to the west (Hyperion; Manganese Range) and east (Tethys-Genie) of Abra, along the E–W trending Quartzite Well Fault (Figs. 1 and 2). Along the same fault and about 40 km to the west, the Woodlands prospect consists largely of disseminated magnetite, minor pyrite, galena, chalcopyrite and barite associated with intense chloritic alteration. The Abra polymetallic deposit is hosted in siltstone, dolostone, sandstone and conglomerate of the Irregully and Kiangi Creek Formations but the mineralised zone does not extend above an erosion surface marking the change from fluvial to marine facies in the lower part of the Kiangi Creek Formation (Thorne et al., 2009).

In this contribution, we present the results obtained from petrographic, fluid inclusions and microthermometric studies, S and Pb isotope systematics and Re–Os dating of pyrite samples. We conclude with a review of previous genetic models and propose a new conceptual ore genesis model, based on our data integrated with previous studies of the deposit.

2. Regional geological setting

The Abra deposit is hosted in siliciclastic metasedimentary rocks of the Irregully and Kiangi Creek Formations of the Mesoproterozoic Edmund Group. The Edmund Group and the overlying Collier Group are the youngest depositional elements of the ~1000 km long, northwest-southeast to east-west trending Capricorn Orogen, located between the Archean Pilbara and Yilgarn Cratons (Cawood and Tyler, 2004). The Edmund and Collier Groups are described in Cutten et al. (in press). These authors subdivided these Groups into six depositional packages, the first four for the Edmund Group and packages 5 and 6 for the Collier Group. The packages of the Edmund Group comprise the Yilgatherra, Irregully Formations (Package 1), Gooragoora, Blue Billy, Cheney Springs Formations (Package 2), Kiangi Creek andMuntharra Formations (Package 3), Discovery, Devi Creek, Ullawarra and Cooardoo Formations (Package 4). Following extensive erosion, a depositional hiatus separates the Edmund and Collier Groups.

The structural architecture of the Capricorn Orogen has controlled deposition in the Edmund and Collier Basins, their deformation, the Abra mineralisation and the above-mentioned mineral occurrences, such as Woodlands, Manganese Range, Hyperion, Tethys-Genie and Rhea (Figs. 1 and 2). The early history of the Capricorn Orogen involved the collision of the northern Glenburgh Terrane with the Pilbara Craton during the Ophthalmian Orogeny (2215–2145 Ma), followed by collision of this combined entity with the Yilgarn Craton to the south during the Glenburgh Orogeny (2005–1950 Ma) accompanied by the intrusion of granitic rocks of the Dalgaringa Supersuite (Sheppard et al., 2010, 2011; Johnson et al., 2011a,b). Two further intracratonic orogenic events reactivated these older sutures, the Capricorn Orogeny (1820–1770 Ma) with intrusion of the Moorarie Supersuite, followed by the Mangaroon Orogeny (1680–1620 Ma) with intrusion of the Durlacher Supersuite. During a subsequent period of rifting from ~1620–1465 Ma the Edmund Basin developed from normal movement reactivation of the basement faults to the formation of a series of half grabens. In the closing stages of the deposition the Edmund Group was intruded by mafic sills (Narimbunna Dolerite, ~1465 Ma; Wingate, 2002). During and following a depositional hiatus lasting as long as 395 myrs, the Edmund Basin was uplifted and deformed during the Mutherbukin Tectonic Event (1320 Ma–1170 Ma) (Johnson et al., 2011a,b, 2012, 2013). Erosion of the Edmund Group supplied detritus to the overlying Collier Group, which may represent a foreland basin, and which is age-constrained by intrusion of Kulkatharra Dolerite sills dated ~1070 Ma, probably part of the Warakurna Large Igneous Province (Wingate, 2002; Wingate et al., 2004). Some of these sills that intruded the basal Collier Group succession show peperitic textures (Martin, 2003) suggesting that the complete Collier Group may have been deposited in a short period of time around 1070 Ma. Subsequent tectonic activity then deformed the Edmund Basin during the Edmundian Orogeny (1030–950 Ma) (Sheppard et al., 2007). The hydrothermal nature of the Abra deposit indicates emplacement during significant faulting events. Geochronology indicates correlation with the Mutherbukin Tectonic Event and the Edmund Orogeny. The stratigraphic placement and geochronological dating associated with formation of the Abra deposit is discussed below.

A seismic survey, the Capricorn Seismic Survey (Johnson et al., 2011a,b, 2012), located approximately 230 km west of Abra, extends from the Pilbara Craton across the Capricorn Orogen to the Yilgarn Craton (Figs. 1 and 3). This imaged the collisional sutures and major faults extending to and offsetting the Moho. One of the major faults, the Lyons

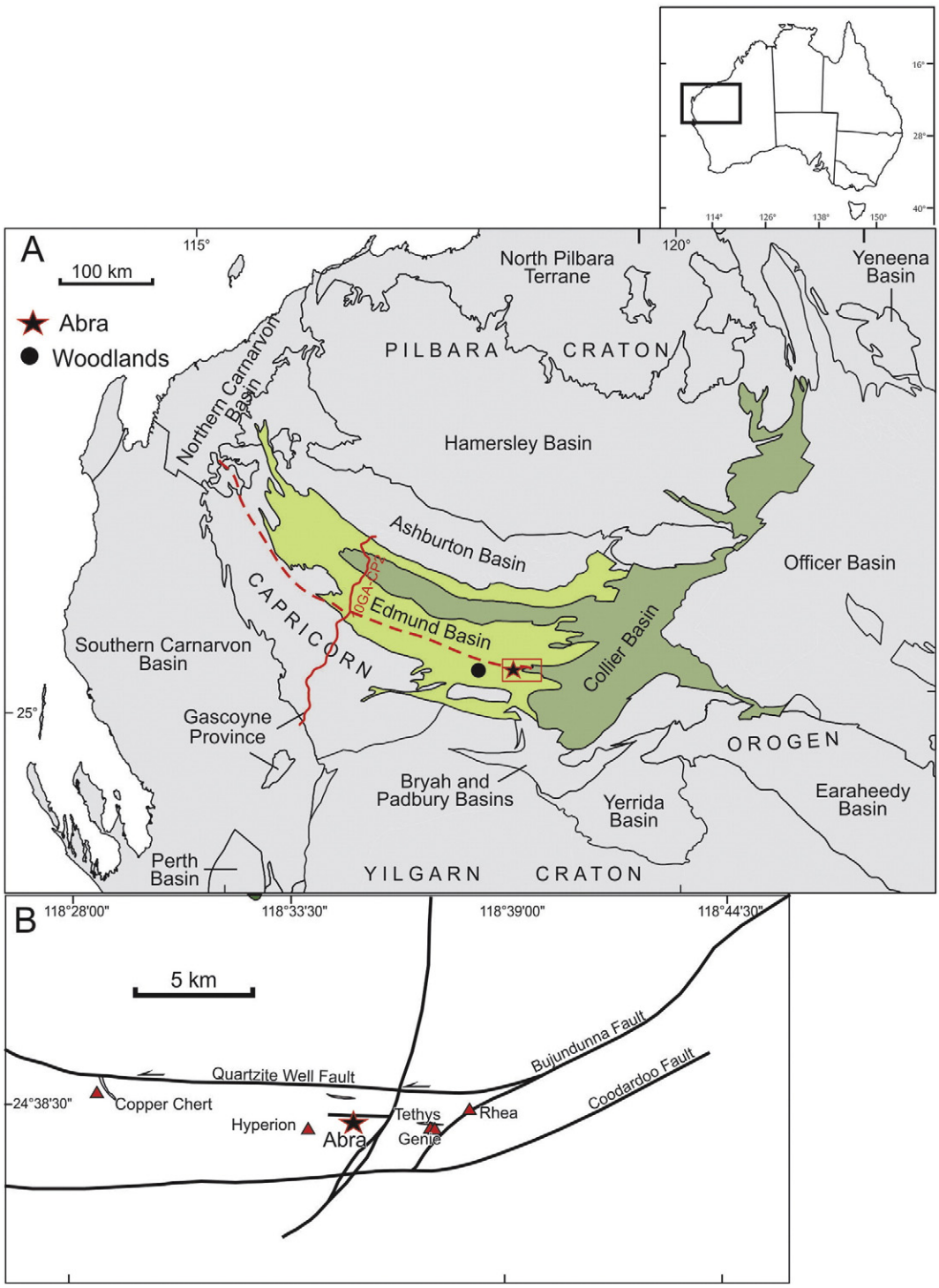

Fig. 1. A) Edmund and Collier basins in the Capricorn Orogen and position of the Abra and Woodlands deposits; also shown is the seismic line (10GCA-CP2; seismic profile is shown in Fig. 3), dashed line represents the Lyons River–Quartzite Well Fault; B) simplified structural setting and control of the Abra deposit and of mineral occurrences within the Abra cluster (position of B is shown by the rectangle in A).
Modified after Johnson et al. (2012), Cutten et al. (in press).

River Fault, extends east becoming the Quartzite Well Fault (Fig. 1), which is a most significant structure for the Abra mineralisation.

3. The Abra mineralisation

The Abra mineral system is characterised by a funnel-shaped brecciated zone, interpreted as a feeder pipe, overlain by stratiform–stratabound mineralisation (Fig. 4). The mineralisation consists of chemical sediments dominated by Fe oxides and barite underlain by sulphides, informally known as Red Zone and Black Zone, respectively. The Red Zone is characterised by banded jaspilite, hematite, galena, pyrite, quartz, abundant barite, and siderite. The jaspilite and hematite cause the predominant red colouration. Barite is a major component and in places forms massive zones. The Black Zone consists of veins and rhythmically banded Pb, Zn and minor Cu sulphides, locally intercalated with laminated and/or brecciated hematite, magnetite, Fe-rich

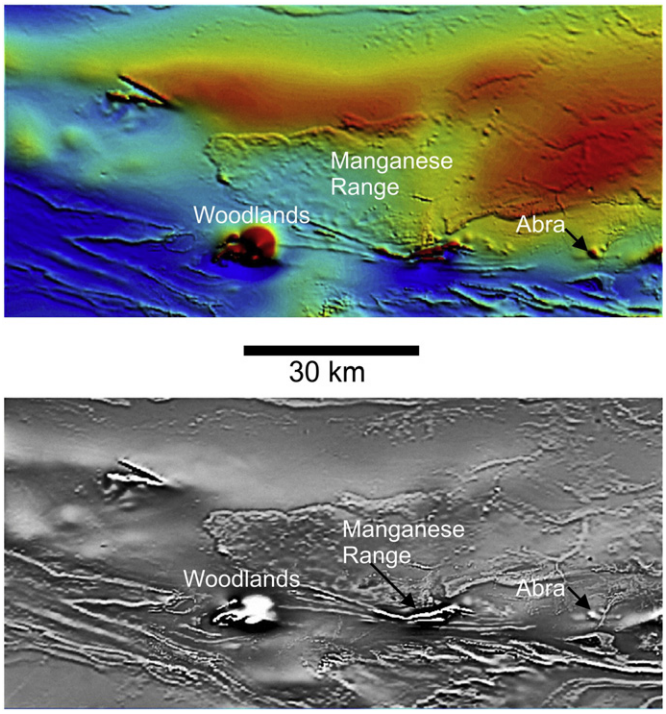

Fig. 2. Aeromagnetic maps of the Abra-Manganese Range-Woodlands area, note the small size of the Abra magnetic anomaly compared to that of Woodlands, whereas Manganese Range is linear. These anomalies can be interpreted as a carbonatite plug or a larger breccia pipe (or both) for Woodlands, a SEDEX style chemical sediments for Manganese Range and the "smaller" breccia pipe for Abra. These aeromagnetic anomalies showing the stark contrast between the three systems also point to a still poorly known much greater target at Woodlands.

carbonate, barite and scheelite. The ore minerals are galena, sphalerite, pyrite, with minor tetrahedrite, chalcopyrite and scheelite. It is worth mentioning that scheelite is known to be commonly associated with W-bearing evaporitic brines (e.g., Searles Lake, California, Carpenter and Garret, 1959), while in some systems, such as Broken Hill (Australia) where evaporites are common, scheelite occurs in calcareous rocks (Plimer, 1994, 2006). In both zones, laminations and bands of ore minerals, Fe oxides, barite and quartz commonly exhibit colloform textures. Below the Black Zone is the Stringer Zone (the above-mentioned feeder breccia pipe), which locally merges with the Black Zone and consists of a stockwork of Fe-carbonate-quartz, barite, pyrite, magnetite and chalcopyrite veins and disseminations, with fluidisation and/or jigsaw textures that cut through a wider alteration envelope of chlorite and siderite in rock units of the Irregully Formation.

The Abra mineral system is characterised by several overprinting phases of hydrothermal activity, from several stages of brecciation and fluidisation, barite and sulphide veining to barren low-temperature chalcedonic (epithermal regime) veining. Hydrothermal alteration minerals include multi-stage quartz, chlorite, prehnite, Fe-rich carbonate and albite. Albite (Na metasomatism, due to evaporitic contribution?) is an early alteration phase, whereas Fe-rich carbonate is a late phase. The repetitive nature of the hydrothermal system, fracturing, multiple overprinting of hydrothermal mineral phases and ore minerals, makes the identification of each phase of hydrothermal activity and paragenetic studies, very difficult.

Table 1
Abra deposit.
Indicated and inferred mineral resource.

Domain	Cutoff grade	Category	Million tonnes	Pb (%)	Ag (g/t)	Cu (%)	Au (g/t)	Zn (%)
Lead	2.5% Pb	Indicated	33	4.1	10	0.13	0.06	0.1
		Inferred	60	3.9	10	0.12	0.04	0.1
		Total	93	4.0	10	0.12	0.05	0.1
Copper–gold	0.4% Cu	Indicated	4	0.4	5	0.59	0.56	0.0
		Inferred	10	0.3	4	0.63	0.47	0.0
		Total	14	0.3	4	0.62	0.49	0.0

The lead and silver mineralisation interpretation was constructed using a 2.5% lead cutoff and the estimation was completed using Ordinary Kriging. The copper and gold mineralisation interpretation was constructed using a 0.4 g/t copper cutoff and the estimation was completed using Ordinary Kriging.
Mineral Resource Statement as at 14 May 2008; from Abra Mining Ltd, Quarterly Report, June 2011, submitted to Australian Stock Exchange.

3.1. Petrography

Petrographic analysis of core samples was carried out by conventional optical transmitted and reflected light microscopy. Drill holes from which samples examined were collected include AB 23, 24, 28, 43, 50, 56 and 59. A total of 3700 m was logged from the above drill holes. A representative schematic log showing the zones of the mineralisation is selected from drillhole AB31, shown in Fig. 5. In the pages ahead we present descriptions and petrographic analysis of selected features of representative sections of drillcore, with the aim of illustrating the complexity of the Abra mineral system. The drillholes examined all intersected the Red and Black Zones, the stockworks of the Stringer Zone, ending in extensively chloritised siltstone country rocks.

3.1.1. The Red Zone

The Red Zone, as intersected in the studied drillcore, ranges in thickness from about 40 m to 110 m and typically exhibits several generations of microcrystalline quartz, jasperoidal material, carbonate, siderite, barite and hematite, forming banded and/or colloform aggregates. The quartz is commonly chalcedonic or forms crack-seal veinlets of fibrous quartz, locally associated with chlorite. Banded jasper is also associated with fractured coarse quartz (fractures healed by fine chalcedonic quartz). This quartz may be of late generation and is interbanded with or replaces small bands of jasper-magnetite. Late euhedral pyrite overprints the magnetite. In other places, the banded material is flanked by a quartz–magnetite–siderite assemblage, associated with prehnite sheafs. The banded jasper replaces the hosting siliciclastic rock. Hematite and jasperoidal material are dominant, hence the red colouration of the Red Zone. Relicts of the host lithology comprise lithic arenite and polymitict conglomerate, in places cut by neptunian dykes, in the upper stratigraphic levels.

Large euhedral barite crystals (2–3 mm to 7–8 mm long) are probably of late generation and are generally associated with hematite. Siderite and quartz replace the euhedral barite. Barite is a major constituent of the Red Zone, locally attaining up to 49% of the core examined by Vogt and Stumpfl (1987). Bands of subhedral magnetite occur together with hematite, with the former overprinting the latter. Hematite also occurs as colloform and rhythmically banded microbands with ooid-like structures, overprinted by magnetite. The internal fabric of the hematite ooids, strongly resemble those that are commonly found in iron formation by chemical precipitation of cryptocrystalline iron oxyhydroxides on seed grains on the seafloor, from seawater enriched with Fe, Al and Si (Bhattacharyya and Kakimoto, 1982; Sturesson et al., 2000). In one hole (AB28) at about 366 m of core depth, a 10-cm thick pale-green chert layer consists of mono- and poly-crystalline round to angular quartz, embayed quartz phenocrysts, minor microcline detrital fragments and some mica and plagioclase fragments (<1 to 3 mm across) in a fine-grained matrix of quartz, mica, overprinted by euhedral barite crystals. This pale-green chert is cross-cut by quartz–chlorite, quartz–siderite, and is probably an immature volcanic sandstone, originated from a felsic protolith (volcanic ash?).

A selection of these features is shown in Figs. 6 (jasper and barite), 7 (barite, hematite, magnetite) and 8 (rhythmically banded jasper, hematite and quartz, barite, albite, hydraulic fracturing).

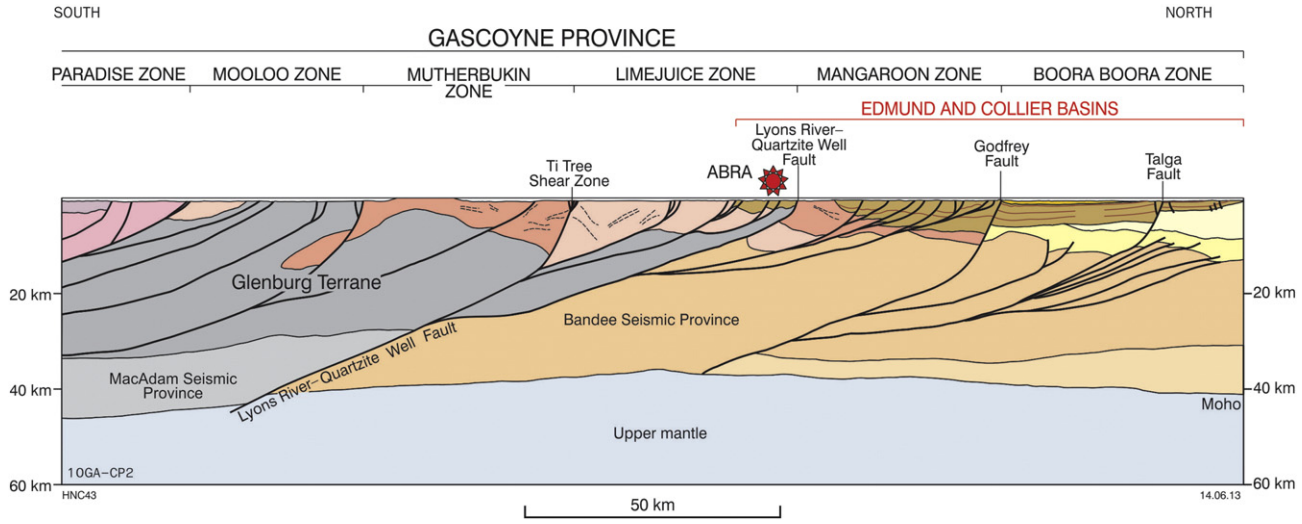

Fig. 3. Capricorn Orogen Seismic Survey transects (see Fig. 1 for position) showing trans-crustal major faults that reach the Moho; the Lyons River–Quartzite Well fault system is the major fluid conduct for the Abra-Manganese Range-Woodlands and other occurrences. The seismic transect is after Johnson et al. (2012, 2013).

3.1.2. The Black Zone

The Black Zone is generally from about 30 to 100 m thick, underlies and locally overlaps with the Red Zone. The Black Zone is dominantly characterized by laminated or banded hematite and magnetite, associated with pyrite–galena–chalcopyrite and quartz + barite layers and veins. The banding exhibits colloform or crenulated textures. Chalcopyrite tends to occur as inclusions in galena, whereas the latter penetrates microfractures in pyrite and is probably a late phase. Individual blebs of chalcopyrite also appear as a late sulphide phase. The siliciclastic protolith is generally replaced by massive quartz ± barite aggregates with abundant sericite veins and as interstitial mineral. Galena may be present in fractures (visible in hand specimen) and associated with disseminated pyrite. Where mineralised with pyrite there is also abundant quartz, carbonate and sericite. Also present is euhedral albite associated with silica and sericitic alteration. Barite forms very coarse and euhedral crystals that are partly replaced by pyrite and carbonate, or quartz–albite and late carbonate. A possible paragenetic sequence (older → younger) is: albite → barite → galena → sericite. Fractures are in places filled with semi-massive aggregates of pyrite–galena–chalcopyrite, associated with coarse-grained quartz euhedral crystals and coarse siderite. The sulphides penetrate fractures and interstices of the quartz and siderite. As pointed out by Vogt and Stumpfl (1987), Fe oxides and sulphides laminations are commonly fractured and veined by later stages of sulphides and Fe oxides. Also, typical of the Black Zone are "wriggly" skarn style textures (Kwak, 1987), characterized by galena–pyrite–hematite "wriggles", locally interbanded with barite–siderite–galena.

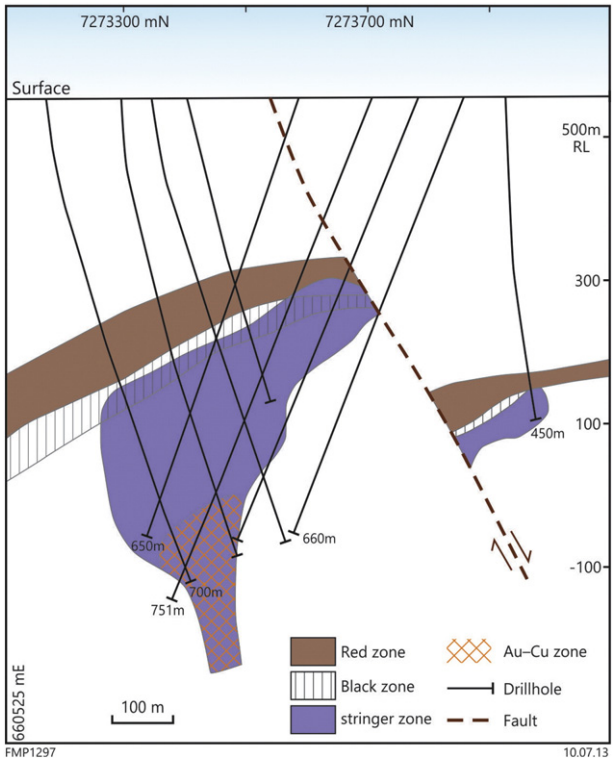

Fig. 4. Geological N–S cross-section modified and simplified from drillholes along line 660525 E (modified from a power point presentation by Abra Mining Ltd., in Beijing, China Mining 2008), illustrating the geometry of the deposit. The white area of the figure represents undefined chloritic altered host rocks.

The host lithologies are variably replaced by ore and alteration minerals. For example, silica replacement of a laminated siliciclastic rock, later impregnated by Fe oxides and sulphides comprises weakly banded quartz aggregates, fine-microcrystalline bands to coarse-grained veins and/or replacements by cockade quartz. One band consist of partly silicified siliciclastic (arenite) with galena blebs filling open spaces and platy hematite filling microfractures. In another example, quartz–calcite veins, with face-control quartz growths (along the crystal c-axes and perpendicular to the vein walls and the cavity) into open spaces, filled by later stage calcite, whereas galena and sphalerite infiltrate crystal boundaries and microfractures. Rhythmic bands can be seen of hematite + carbonate (?ferroan dolomite or siderite) and coarse quartz + calcite or fibrous quartz aggregates. These subparallel veins or quartz/carbonate infills possibly replace pre-existing sedimentary laminae. Chlorite also occurs as a late alteration phase replacing galena and magnetite and as sinuous veinlets cutting through the siliciclastic protolith, or replacing lithic clasts and related matrix. In other instances chlorite occurs together with albite bordering the sulphides. Chlorite is of the Fe-rich variety (purple birefringence). A selection of key features of the Black Zone is shown in Figs. 9, 10 and 11.

3.1.3. The Stringer Zone (feeder or breccia pipe)

The Stringer Zone is made up of variably brecciated and veined chloritised and silicified clastic host rocks (siltstone and arenite mainly). The Stringer Zone lies below the Black Zone and may extend for more than 400 m of depth, with a metal association dominated by Cu, Au and Bi. The Stringer Zone is estimated to contain about 150 Mt of metal sulphides, including 0.13 g/t Au (Cooper et al., 1998). The lower

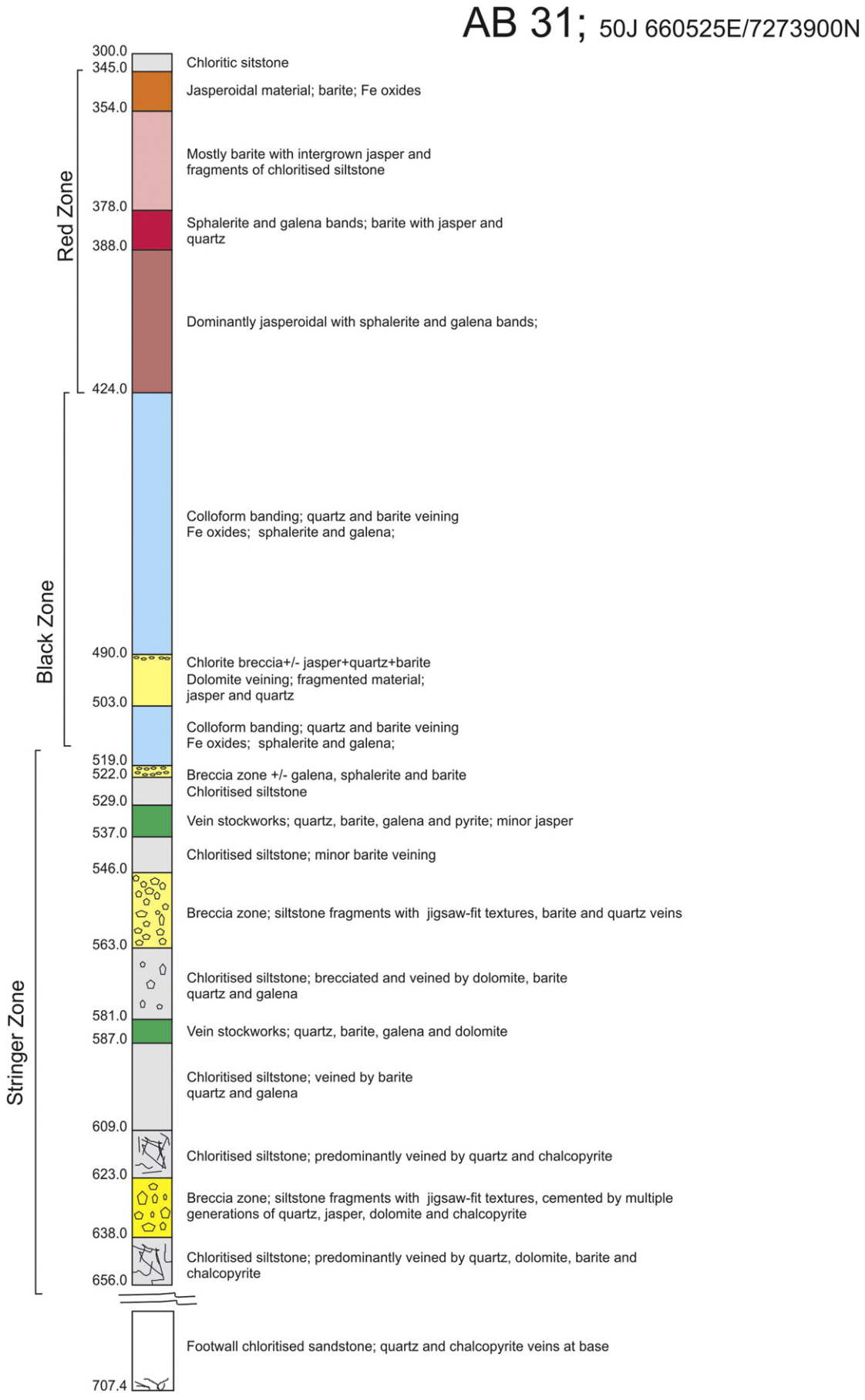

Fig. 5. The complexity of the Abra mineral system is well illustrated by this simplified core log of drillhole AB31.

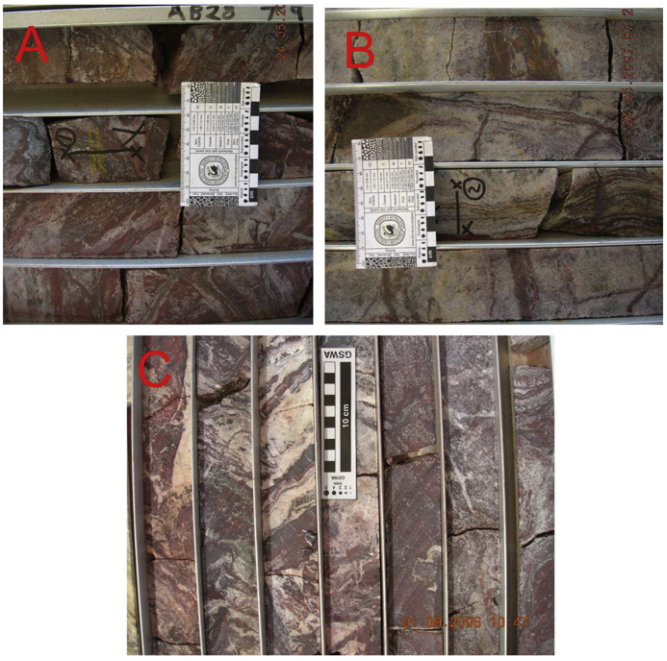

Fig. 6. Examples of Red Zone textures; A and B Drillhole AB28, A (326 m) shows a dominantly jasperoidal rock with barite, quartz, hematite and magnetite bands and veins with several generations of quartz: microcrystalline quartz, granular, chalcedonic-carbonate; B (346.8 m) shows a weakly banded texture with coarse-grained intergrown aggregates of quartz-siderite forming microbands; siderite also occurs interstitial between quartz crystals; C) Drillhole AB31 (346 m), dominantly jasperoidal material intercalated with colloform quartz and Fe oxides.

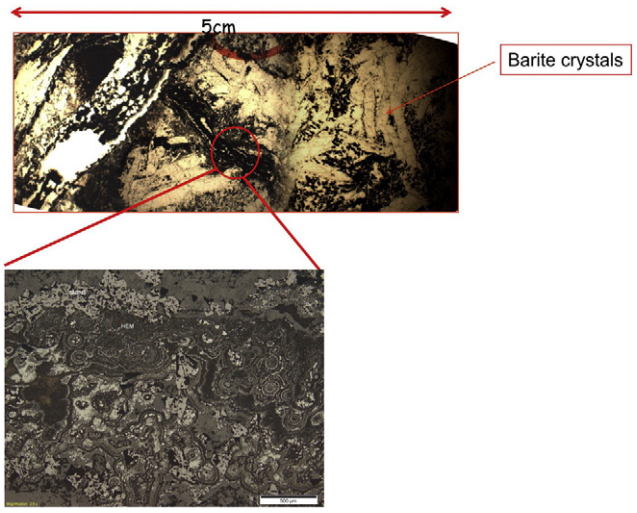

Fig. 7. Euhedral barite crystals, from 2–3 mm to 7–8 mm long, associated with hematite and magnetite; the reflected light photomicrograph shows that hematite forms colloform microbands with concentric peloid-like structures, locally with magnetite in the core, euhedral magnetite is late and overprints the hematite.

part of the Stringer Zone is enriched in Cu and Au. As stated previously, according to the Abra Mining website (http://www.abramining.com.au/), there are about 14 Mt of mineralisation containing and average gold grade of 0.5 g/t. The petrographic descriptions below illustrate the complexity of the Stringer Zone mineralisation.

In drillhole AB28 at about 541 m, is a lithic breccia with quartz, chert, chloritized lithic fragments and clasts, cut by several generations of veinlets of the same material. Cement material is microcrystalline quartz with a chloritised matrix. Locally, galena, pyrite, chalcopyrite and magnetite blebs, fill cracks and replace along crystal boundaries the main mineral phases. At a core depth of 544 m, the lithic breccia exhibits a coarse-grained assemblage of quartz crystals and Fe-rich carbonate (siderite or ferroan dolomite?), with relics or patches of immature siliciclastic rock. Both the coarse quartz and the Fe carbonate are hydrothermal and replace the original siliciclastic rock. Quartz crystals have abundant secondary fluid inclusions (inclusions transgress crystal boundaries); primary inclusions (L + V) also present. The brecciated host siliciclastic also contains hematite + quartz + sericite + carbonate veinlets, flanked by brecciated quartz–chlorite assemblage. The sericite in the quartz–carbonate vein is a late phase. Quartz + galena + chalcopyrite occur in the centre of these veinlets and filling fractured carbonate. Another curious feature that occurs in the Stringer Zone is the presence of hematite atoll-like shapes, centrered around a spheroid, about 27 μm in diameter (microbial?).

3.1.4. Footwall rocks

The footwall rocks that are cut by the Stringer Zone consist of laminated mudrocks, composed of thin laminae of silt-grade quartz grains with angular quartz fragments in a micaceous clay matrix with incipient alteration to chlorite. This chlorite occurs as unevenly distributed irregular patches, in microfractures and along margins of veinlets. The mica flakes are oriented sub-parallel to laminations. Cross-cutting cm-wide carbonate veins are present and generally exhibit two sections: coarse-grained carbonate crystals and very fine carbonate material. Chalcopyrite and minor galena are contained in one quartz veinlet. Pervasively silicified rock, with minor carbonate and with abundant galena and minor chalcopyrite and pyrite filling interstices and locally replacing the quartz grains are marginal to the Stringer Zone. Micaceous and chloritised assemblage with very fine quartz grain laminations are dotted with euhedral (almost porphyroblastic) carbonate crystals that overprint the chlorite matrix and are cross-cut by sinuous carbonate veinlets.

3.2. Fluid inclusions

3.2.1. Samples and methodology

Fluid inclusion studies were undertaken on doubly-polished thin sections (sample Nos. 187836 and 197707). The first step of the study involved a detailed fluid inclusion petrographic study to identify primary, pseudosecondary and secondary fluid inclusions and to determine the relative timing a different populations of inclusions. All subsequent microthermometric and laser Raman microprobe studies were carried out on individual fluid inclusion assemblages that were simultaneously trapped within the crystals.

Microthermometric data were obtained using a Linkam MDS 600 heating-freezing stage, which was calibrated with a series of synthetic fluid inclusions of known composition. A heating rate of 1 °C per minute was used to record phase changes below 30 °C, whereas a heating rate of 5 °C per minute was used for phase changes above this temperature. Hence, low-temperature phase changes are accurate to ±0.2 °C, whereas temperatures above 30 °C have an estimated accuracy of ±2 °C. Salinity, mole fractions and bulk density of each inclusion were calculated using the MacFlinCor programme (Brown and Hageman, 1995). The salinity of the Ca-bearing fluids was calculated using the method of Chi and Ni (2007). Laser Raman spectra of fluid inclusions were recorded on a Dilor© SuperLabram spectrometer equipped with a holographic notch filter, 600 and 1800 g/mm gratings, and a liquid N_2 cooled, 2000 × 450 pixel CCD detector. The inclusions were illuminated with 514.5 nm laser excitation from a Melles Griot 543 Series argon ion laser, using 5 mW power at the samples, and a single 30 second accumulation. A 100X Olympus microscope objective was used to focus the laser beam and collect the scattered light. The focused laser spot on the samples was approximately 1 μm in diameter. Wave numbers are accurate to ±1 cm^{-1} as determined by plasma and neon emission lines. For the analysis of CO_2, O_2, N_2, H_2S and CH_4 in the vapour phase, spectra were recorded from 1000 to 3800 cm^{-1}. The detection

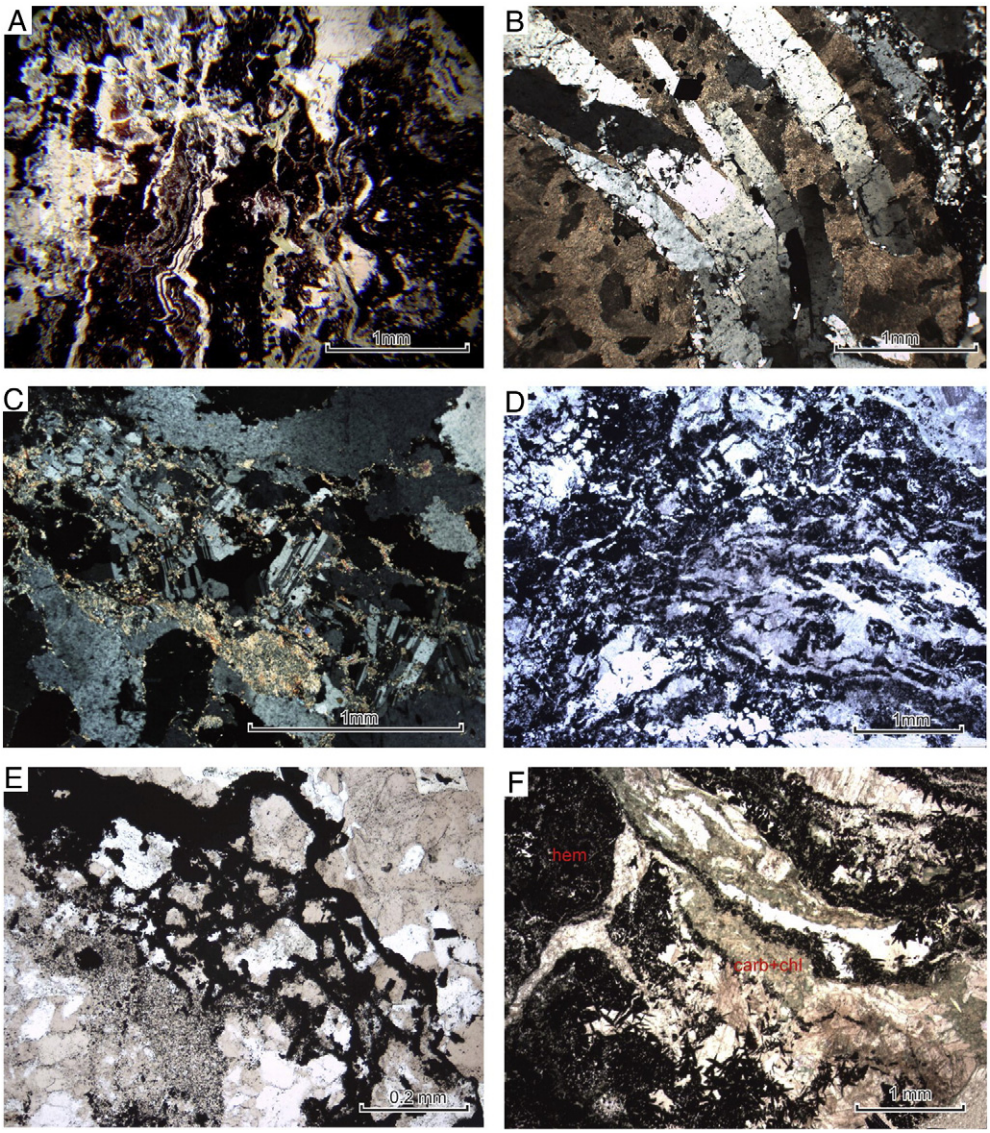

Fig. 8. Photomicrographs of samples from the Red Zone; a) 187836 (AB28, 371 m) rhythmically banded jasper, hematite and quartz, plane polarised light; b) 187836 (AB28, 371 m) barite crystals embedded in siderite, crossed polarised light; c) 187840 (AB28, 383.8 m) albite and sericite alteration, crossed polarised light; d) 187841 (AB28, 319 m) banded siderite and hematite and patches of chalcedonic quartz, polarised light; e) 187846 (AB28, 489 m) hematite filling microfractures induced by hydraulic fracturing in microcrystalline quartz, plane polarised light; f) 197711 (AB56, 445 m) chlorite and carbonate alteration overprinting quartz–feldspar granular assemblage, plane polarised light.

limits are dependent upon the instrumental sensitivity, the partial pressure of each gas, and the optical quality of each fluid inclusion. Raman detection limits are estimated to be around 0.1 mol% for CO_2, O_2 and N_2, and 0.03 mol% for H_2S and CH_4 and errors in the calculated gas ratios are generally less than 1 mol%. Details of microthermometric analyses are given in Appendices 1 and 2.

3.2.2. Results

3.2.2.1. Sample 187836 (Red Zone). This sample is characterised by a red-brown carbonate vein ~3–5 mm thick near the centre of the slide. This is surrounded by red jaspilite and hematitic sediments and minor green clumps of chlorite (up to 2 mm diameter). The red layers are cut by subparallel, stigmatic, barite veins. The early carbonate vein is cut by narrow crack-seal type, dolomite–chlorite veins ~1 mm thick. This latter vein is overprinted by irregular quartz and barite crystals up to 5 mm in diameter. No fluid inclusions of a suitable size could be found in the early carbonate vein. The subparallel, barite veins contained trails of pseudosecondary or secondary fluid inclusions mostly perpendicular to the walls of the veins (Fig. 12a). They are irregular to rounded in shape with no obvious signs of necking and ranged in size up to about 25 μm in diameter. The majority of these inclusions contain only liquid, but a few contain up to 5 vol.% vapour. Rare vapour-rich inclusions are rarely observed. The presence of liquid-only fluid inclusions indicates entrapment in the low-temperature phreatic zone at temperatures below 50 °C. The inclusions with a small amount of vapour were most likely modified by heating during subsequent burial and the rare vapour-rich inclusions most likely result from leakage of the liquid-rich inclusions.

The crack-seal carbonate veins contain rare trails of pseudosecondary to secondary fluid inclusions (Fig. 12b). Once again these are mostly liquid-only inclusions with a few rare inclusions containing up to 5 vol.% vapour. Rare vapour-rich inclusions are thought to result from leakage. The quartz crystals contained abundant trails of secondary fluid inclusions up to 30 μm in diameter (Fig. 12c). They are irregular to rounded in shape and have relatively constant liquid:vapour ratios of 5–10 vol.%. Rare three-phase inclusions containing a small crystal of dolomite (identified by Raman analysis) were also observed. The barite crystals contain abundant trails of primary to pseudosecondary fluid inclusion up to 40 μm in diameter (Fig. 12d). Once again the majority of inclusions are liquid-only suggesting entrapment within the low-

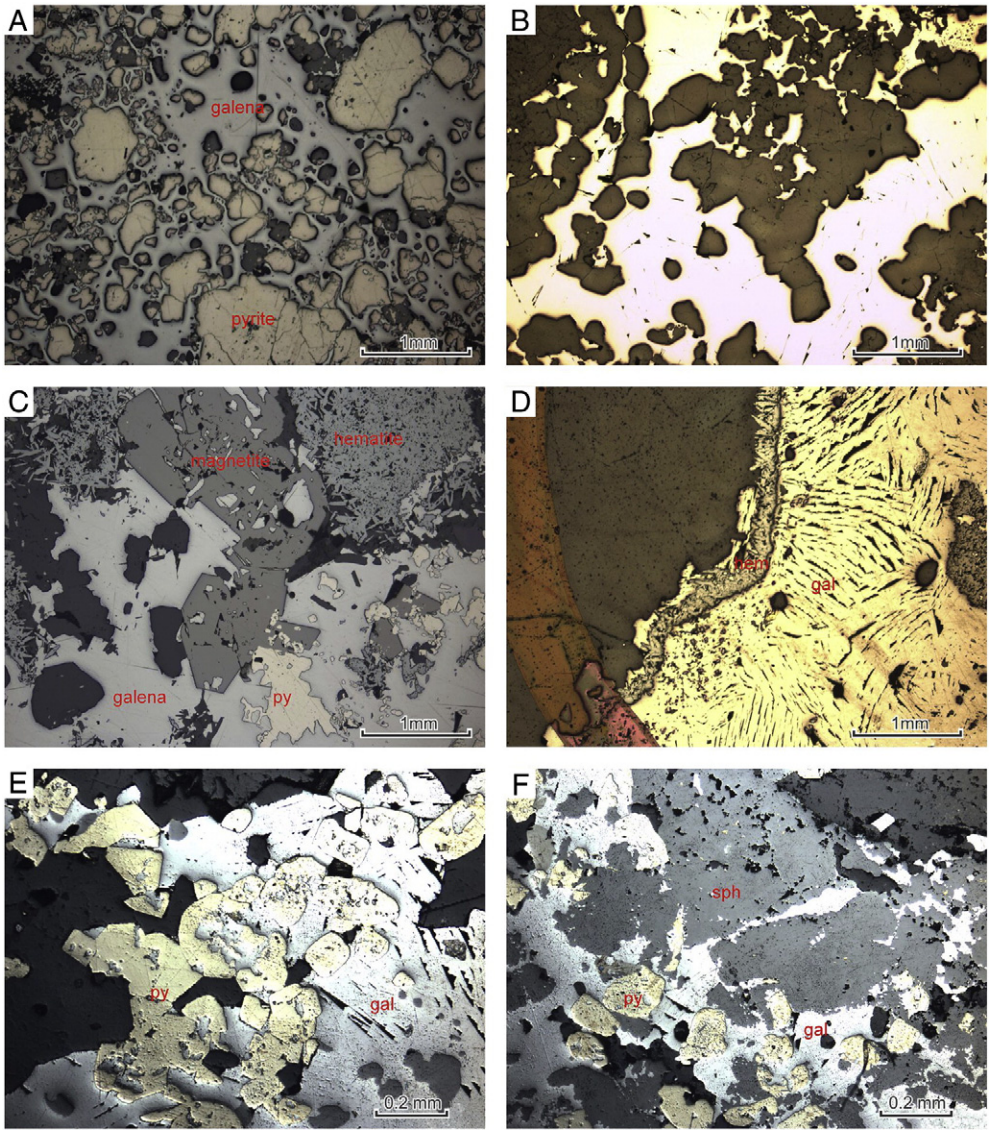

Fig. 9. Reflected light photomicrographs of samples from the Black Zone; A) 187843 (AB28 drillhole, 426.5 m), galena and pyrite assemblage replacing a siliciclastic host; B) GSWA 187856 (AB28 drillhole, 669.3 m) galena replacing a granular quartz mosaic of a pervasively silicicified silicified host rock; C) 187843 (AB28 drillhole, 426.5 m), semi-massive sulphides (galena and pyrite) and Fe oxides (hematite and magnetite) replacing a siliciclastic host; D) 187829 (AB24 drillhole, 503.8 m) coarse-grained galena rimmed by hematite, here galena is slightly deformed, perhaps accounting for its unusual colour; E) and F) GSWA 197706 (AB56, 383.5 m) zone of massive sulphides comprising and assemblage of sphalerite, pyrite and galena Mineral abbreviations: py pyrite, gl galena, hem hematite, mg magnetite.

temperature phreatic zone at temperatures below 50 °C. Some inclusions contain small vapour bubbles with liquid:vapour ratios typically less that 10 vol.%. Rare dark, vapour-rich fluid inclusions have either leaked or contain $CO_2 \pm N_2 \pm CH_4$ (identified by Raman analysis).

3.2.2.2. Microthermometry. Due to the nature of the inclusions in the early carbonate and stigmatic barite veins microthermometric analysis was only carried out on inclusions in the larger quartz and barite crystals. As mentioned above the presence of liquid-only inclusions in the barite indicates entrapment in the low-temperature phreatic zone at temperatures below 50 °C. After some heating during burial, some of the fluid inclusions in barite may have re-equilibrated to form two-phase inclusions that have only somewhat consistent liquid:vapour ratios. However, microthermometry was performed on these inclusions to check that they contain essentially the same fluid as in the quartz crystals. As barite is a softer mineral than quartz the all liquid-inclusions may be stretched during cooling and so homogenisation temperatures were recorded first in order to avoid this problem. Total homogenisation temperatures for vapour-bearing inclusions in both the quartz and barite are shown in Fig. 13a. It can be seen that the values for quartz form a tight cluster with a mode at 165 °C, whereas the inclusions in barite exhibit a large scatter of homogenisation temperatures varying from 59 °C to 201 °C. This large scatter of homogenisation temperatures indicates that the inclusions in barite have undergone either leakage or stretching after initial re-equilibration. Eutectic temperatures as low as −45.6 °C were observed upon warming after cooling the samples. However, the data indicate that two different fluids have been trapped in both the quartz and barite crystals. The low eutectic temperatures indicate the presence of a Ca-bearing and possibly Mg-bearing (due to the observed dolomite daughter crystal) fluid while eutectic temperatures around −21.2 °C indicate the presence of a Na-bearing fluid. For the Ca-bearing fluid ice melting temperatures varied from −2.2 to −9.9 °C while hydrohalite melting varied from −18.0 to −20.6 °C. The calculated salinities are shown in Fig. 13b and vary from 3.7 to 13.8 wt.% NaCl with a mode around 8 wt.% NaCl. The Na-bearing fluid had final ice melting temperatures from −1.3 to −9.6 °C and salinities from 2.2 to 13.5 wt.% NaCl (Fig. 13b) with modes at 3 and 7 wt.% NaCl respectively.

3.2.2.3. Laser Raman microprobe analysis. The vapour phase of fluid inclusions in both barite and quartz were analysed by laser Raman

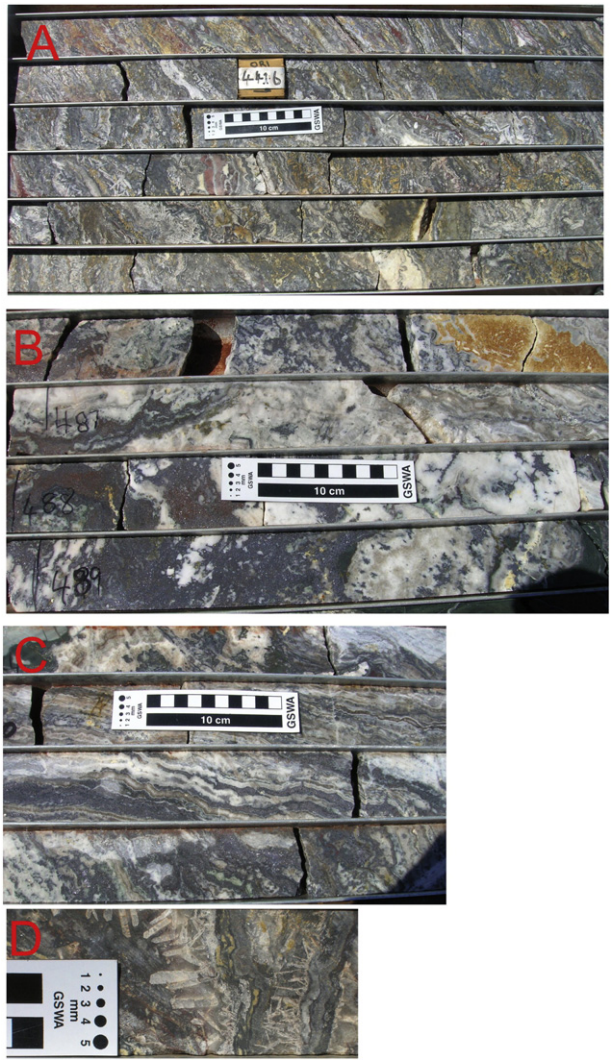

Fig. 10. Photographs of core from the Black Zone, showing key features as follows; a) AB31 drillcore (442 m) rhythmic banding of galena and minor sphalerite, with colloform quartz, overprinted by late barite euhedral crystals; b) AB50 drillcore (487 m) showing galena overprinted by late quartz veining and by barite; c) AB50 drillcore (500 m) slightly contorted rhythmic bands of galena and quartz; d) AB31 drillcore (450 m) shows euhedral barite crystals of late generation cutting through sulphides.

microprobe analysis. Most inclusions contained no detectable gases but a few inclusions with slightly darker bubbles contained CO_2 or mixtures of CO_2, N_2 and CH_4. The majority of gas-rich inclusions contained only CO_2 but a few contained dominantly CO_2 with minor N_2 and CH_4. In one inclusion only N_2 was detected and this is thought to be an inclusion that has leaked and now only contains air. The presence of CO_2 and other gases in some inclusions may indicate the passage of diagenetic or metamorphic fluids within the deposit.

3.2.2.4. Sample 197707 (Black Zone). This sample contains relatively large (up to 20 mm diameter) irregular grains of barite in a finer groundmass of barite and pyrite, chalcopyrite, galena and sphalerite. The large barite grains are cross-cut by secondary trails of fluid inclusions (Fig. 14a). Two types of fluid inclusion trails are observed. The first type contain mostly rounded inclusions up to 10 μm in diameter with variable liquid:vapour ratios but are mostly vapour-rich (Fig. 14b). This could indicate trapping of immiscible fluids during boiling or effervescence. The second type contain mostly irregularly-shaped inclusions that are typically either liquid-only or contain less than 5 vol.% vapour (Fig. 14b). This once again suggests entrapment in the low temperature phreatic zone. Rare three phase inclusions containing a solid crystal of dolomite are also observed (Fig. 14c).

3.2.2.5. Microthermometry. Sample 197707 contained many more two-phase, liquid-rich inclusions indicating that most of the inclusions were either trapped at higher temperatures or, more likely, that the sample has been re-equilibrated at a higher temperature. Total homogenisation temperatures for inclusions in the large barite grains are shown in Fig. 14d. The vapour-rich inclusions typically have higher homogenisation temperatures ranging from 288 to 385 °C with the exception of one inclusion at 168 °C which may represent a leaked inclusion. The liquid-rich inclusions homogenised from 150 to 279 °C with a mode at 190–200 °C. All eutectic melting temperatures in sample 197707 were close to −21 °C indicating that the inclusions contained a NaCl dominant fluid. Final ice melting temperatures ranged from −8.2 to −1.2 °C which corresponds to salinities between 2.0 and 11.5 wt.% NaCl (Fig. 11). The spread in salinity indicates that possibly a mixing trend between high and low salinity fluids has occurred. The vapour phase in a number of liquid-rich and vapour-rich fluid inclusions was analysed with the laser Raman microprobe, but no gases were detected in any of the selected inclusions in sample 197707. A 3D plot of temperature of homogenisation vs salinity and depths (Stringer zone, Black Zone and Red Zone) is shown in Fig. 15.

3.3. S isotopes

The sulphur isotopic system shows $\delta^{34}S$ values ranging from 19.4 to 26.6‰ for sulphides (chalcopyrite, pyrite, sphalerite, galena) and from 37.4 to 41.9‰ for barite, relative to CDT (Canon Diablo Troilite) (Vogt and Stumpfl, 1987; Austen, 2007) (Fig. 16). In these works, it is shown that barite values are isotopically heaviest (40.4 to 42.3‰ CDT) and galena values are isotopically the lightest (19.1 to 21.4‰ CDT). Chalcopyrite (20.5 to 26.6‰ CDT) is slightly heavier than galena, pyrite (20.2‰ CDT) and sphalerite (23.1‰ CDT).

The sulphur isotope signature of the sulphides from Abra (and Woodlands) is quite heavy. The S isotope composition of Proterozoic seawater is estimated to be +15 to +16‰ (Lyons et al., 2006; Faure and Mensing, 2005) and the and Abra $\delta^{34}S$ values fall above this value. If sulphides precipitated from a fluid like this, allowing for a small degree of fractionation, sulphur isotope values of around +20‰ would be expected in the sulphides. At temperatures of around 250 °C, the fractionation between sulphides and sulphates (barite) is around +20‰.

Both Abra and Woodlands have very high $\delta^{34}S$ in barite (about +40‰), suggesting that the source fluids were modified Proterozoic seawater in closed systems (Lyons et al., 2006; Faure and Mensing, 2005). These data are consistent with the Abra mineralisation having formed from a Proterozoic seawater or evaporite system, comparable to a "SEDEX" mineral system (Leach et al., 2005; McClung et al., 2007).

Sulphate and sulphide $\delta^{34}S$ values are isotopically heavier for than those obtained at other mineral deposits. However, $\delta^{34}S$ values do correlate with those obtained by Vogt and Stumpfl (1987) for Abra. Vogt and Stumpfl (1987) had a range of 38.4 to 40.8‰ for barites, 20.2 to 24.6‰ for galena, sphalerite and chalcopyrite and 21.1‰ for pyrite values. Sulphate values are slightly heavier than those obtained for Lady Loretta, Mt. Isa Super Basin, Australia (37.4 to 39.7‰) (Vogt and Stumpfl, 1987). Compared to other Northern Australian Proterozoic SEDEX deposits, they are isotopically heavier than many in the Mt. Isa and McArthur Basins. Sulphide and sulphate

values are much heavier than the value estimated for Proterozoic sea water (~16‰; Faure and Mensing, 2005). The overall enrichment in $\delta^{34}S$ (relative to the Primitve Mantle Value of 0.5‰) suggests the ultimate source of sulphur is Proterozoic seawater, which is enriched in $\delta^{34}S$ relative to the mantle. The $\delta^{34}S$ of barite approximates the $\delta^{34}S$ of

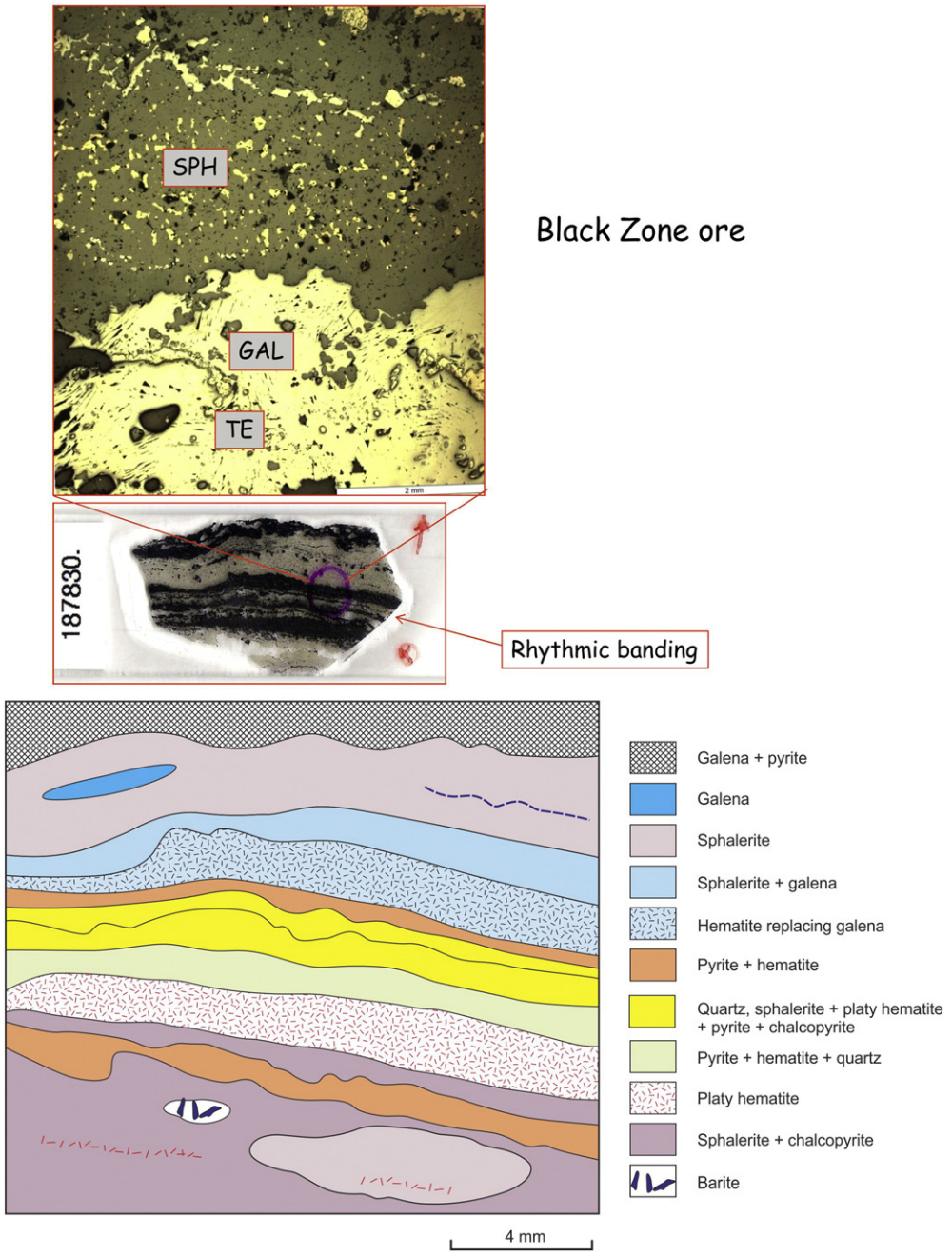

Fig. 11. AB31 drillhole (717 m) photomicrograph in reflected light showing sphalerite (SPH) with chalcopyrite inclusions (chalcopyrite disease; due to reaction of the Fe from the sphalerite with Cu ions transported in hydrothermal fluids; see Eldridge et al., 1988) and galena (GAL), associated with minor tetrahedrite (TE); rhythmic banding at thin section scale (187830), somewhat simplified complexity of this banding shown below the thin section.

sulphate in brine, which is seawater, or modified seawater, with only a small positive sulphur isotope fractionation (1.65‰) relative to the brine.

The $\delta^{34}S$ values of sulphides and their relationship to depth, as determined from drillholes, is shown in Fig. 17. According to Austen (2007), galena and chalcopyrite exhibit a positive trend as values increase with increasing depth. The two chalcopyrite values in the Red Zone are isotopically heavier than those in the Stringer Zone. Therefore, chalcopyrite values may become isotopically heavier with decreasing depth. The 3D plots of Fig. 17a, b shows distinct depth-related groups or clusters; chalcopyrite displays a cluster at depths of 250–400 m and two samples at <50 m; galena, on the other hand, is clustered at 50–100 m (together with sphalerite) and between 170 and <200 m, with a single value at 325 m. This distribution could relate to distinct phases of mineralisation (Red Zone, Black Zone and Stringer Zone).

Sulphur isotope thermometry between sulphides and sulphide–barite pairs yielded values ranging from 219 to 336 °C, whereas oxygen isotope thermometry from coexisting pairs (e.g., quartz, chlorite, hematite and magnetite) show a wider range of temperatures, from 228 to 452 °C (Austen, 2007).

3.4. Pb isotopes

As part of this study of suite of galena separates from four different samples (187829, 187840, 197708 and 197711) from the Abra deposit were analysed for lead isotope ratios at the University of Melbourne. The results are presented in Appendix 3. The new analyses have a more restricted spread in $^{207}Pb/^{204}Pb$ than previous analyses (Austen, 2007) from Abra (Fig. 18a) due to a higher analytical precision. In

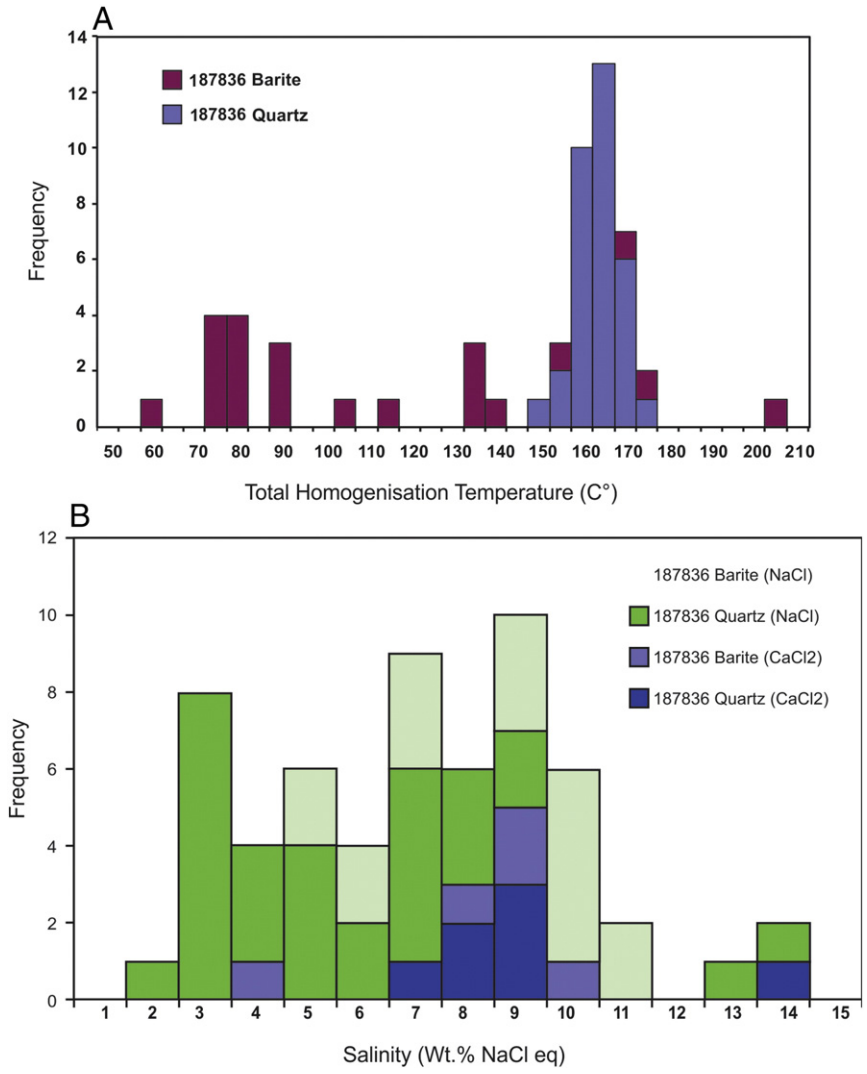

Fig. 12. a) Total homogenisation temperatures for inclusions in quartz and barite crystals in sample 187836; b) Histogram showing the salinity of $CaCl_2$ and NaCl fluids in quartz and barite crystals in sample 187836.

addition, the new analyses yielded somewhat higher $^{207}Pb/^{204}Pb$ values than the previous analyses.

Fig. 18b also compares the new Abra analyses with (mostly) high-precision (double spike and ICP-MS) least radiogenic lead isotope analyses of lead-rich samples (mostly galena) from major Proterozoic mineral deposits in Australia and also with late Paleoproterozoic (~1740 Ma) volcanic-hosted massive sulphide deposits from the Yavapai Province in North America (see Fig. 18 caption for data sources). On Fig. 18a, a model age-μ ($^{238}U/^{204}Pb$) grid has been overlain on the data using the North Australia lead isotope evolution model of Sun et al. (1996). This model gives precise and accurate model ages for many deposits in the North and South Australian Cratons, but is untested in the West Australian Craton.

Using the North Australia model (Sun et al., 1996), the new galena analyses yield model ages of 1760–1740 Ma (and 1754–1739 Ma for the old data). As these model ages are older than the age of the host unit, the North Australian model is not applicable for the Edmund Basin. The model of Cumming and Richards (1975) yields ages of between 1650 Ma and 1628 Ma for the new data (1643–1627 Ma for the old data). Despite the overlap between the Cumming–Richards model age range and the inferred age of the host unit, these ages must be considered preliminary because no local isotopic control exists to establish a lead isotope evolution model for the Edmund Basin. However, the data do suggest a Mesoproterozoic age and are consistent with formation during the early evolution of the Edmund Basin.

Values of μ estimated from the new lead isotope data indicate that Abra lead is more evolved (i.e., has higher μ) than the lead in most other Australian Proterozoic Zn–Pb deposits. These data suggest a crustal source and are compatible with sourcing lead in the Abra deposit from the Edmund Basin, which should be characterised by relatively evolved lead. This hypothesis, however, requires testing through collection of isotopic data and the estimation of lead isotope ratios in the basin at the time of mineralisation.

3.5. Re–Os dating of sulphides and SHRIMP dating of monazite and xenotime

A core sample collected from drillhole AB28 at a depth of 383.8 m was used for Re–Os dating (Appendix 4). This sample is a representative of the feeder zone (Stringer Zone) and consists of primary massive and disseminated pyrite, with a sericite + albite + galena assemblage in microfractures. Also present is euhedral albite associated with silica and sericitic alteration. Barite where present occurs as paragenetically late coarse and euhedral crystals that are partly replaced by pyrite and carbonate, or quartz–albite and late carbonate. From this a single piece of drill core containing massive, coarse-grained pyrite approximately

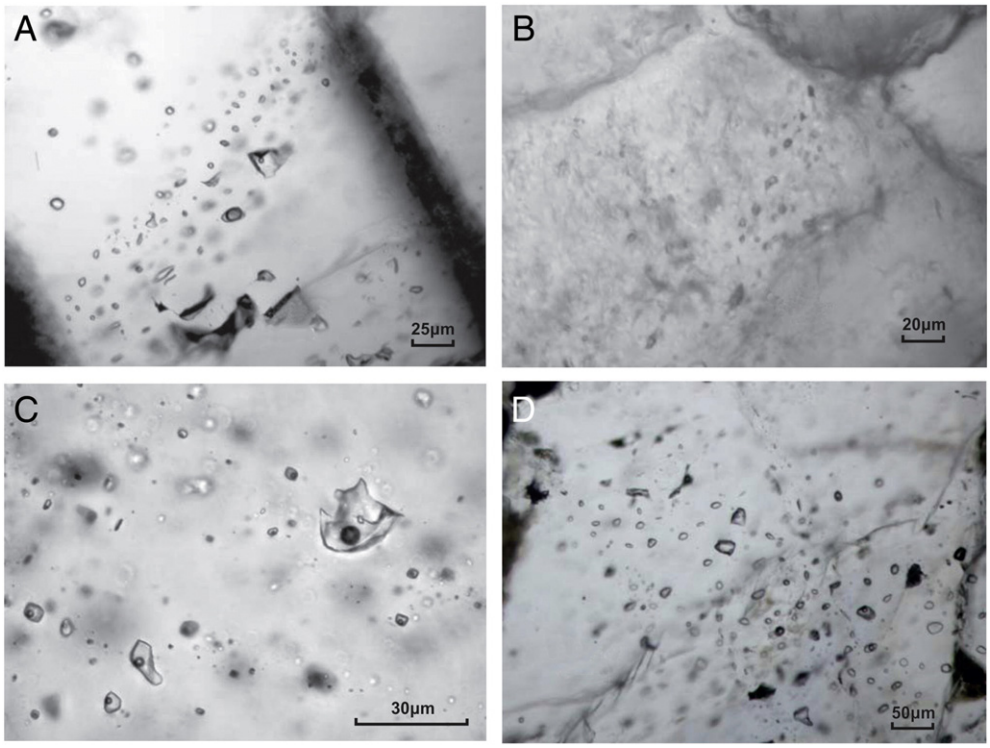

Fig. 13. a) Photomicrograph of thin section 187836 showing fluid inclusion trails in barite containing liquid-only, liquid-rich and vapour-rich inclusions. Scale bar = 25 μm. b) Photomicrograph of thin section 187836 showing fluid inclusion trails in a crack-seal, carbonate vein. Scale bar = 20 μm. c) Photomicrograph of thin section 187836 showing fluid inclusion trails in quartz containing liquid + vapour and liquid + vapour + solid inclusions. Field of view = 130 μm. d) Photomicrograph of thin section 187836 showing liquid-only, liquid-rich and vapour-rich fluid inclusions trails in a large barite phenocryst. Scale bar = 50 μm.

8 cm in length was divided into two sections and processed by metal-free methods to produced pyrite mineral separates (A, B), which were analysed for Re–Os isotopes at the University of Alberta using methods described by Morelli et al. (2010). The pyrite contains 1–3 ppb Re and highly radiogenic Os with $^{187}Os/^{188}Os$ ratios ranging from 42–114 (Table 2). All data yield an age of 1255 ± 150 Ma on a Re–Os isochron

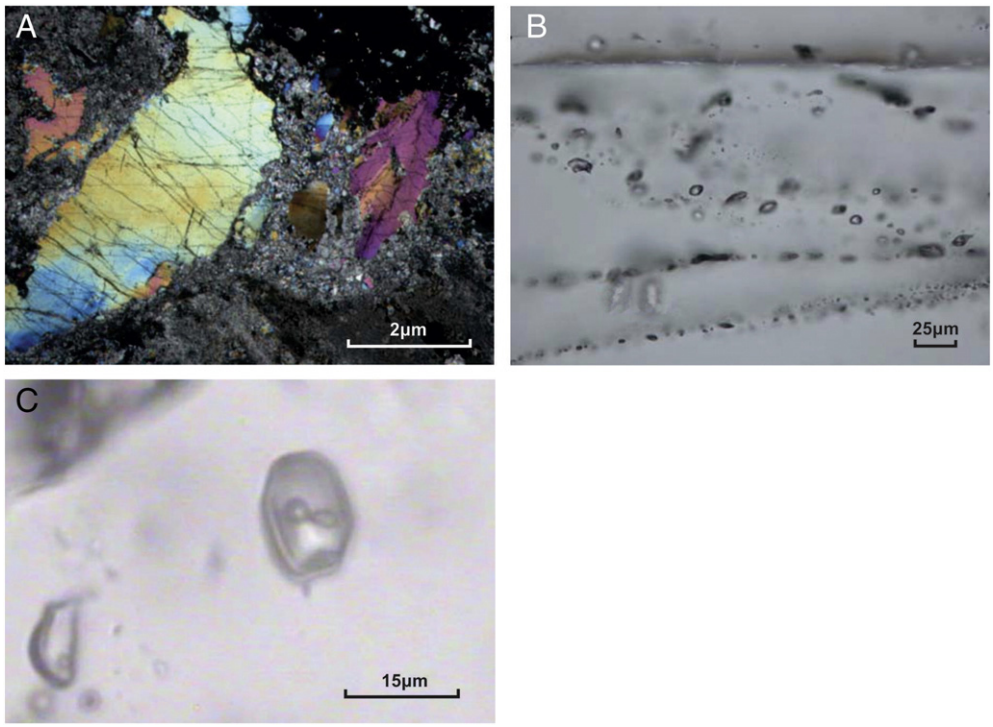

Fig. 14. a) Photomicrograph of thin section 197707 showing cross-cutting fluid inclusion trails in barite crystals. (Cross-polarised light; Field of view = 7.8 mm). b) Photomicrograph of thin section 197707 in transmitted light showing a trail of L + V fluid inclusions (centre) and a trail of predominantly vapour-rich fluid inclusions (bottom). Scale bar = 25 μm. c) Photomicrograph of three-phase fluid inclusion with a small dolomite crystal. Field of view = 65 μm.

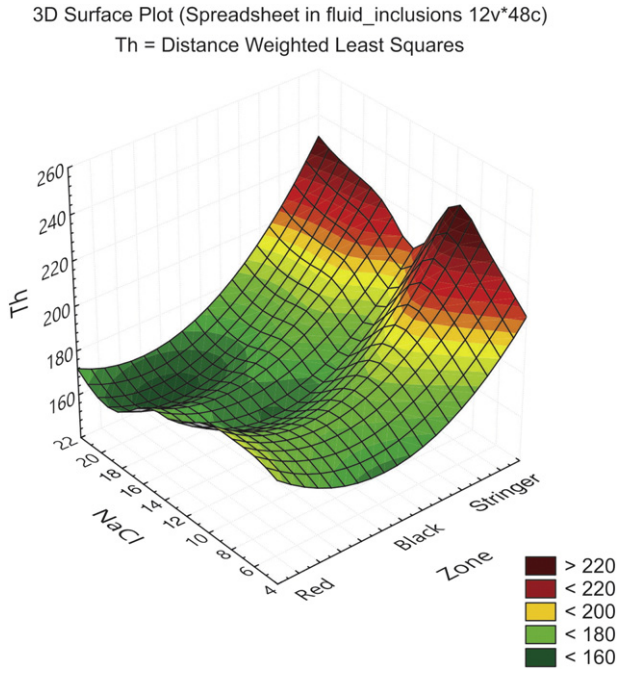

Fig. 15. 3-D plots of temperature of homogenisation (Th) versus salinity (NaCl equivalent), versus depth (m) (data from Austen, 2007); noticeable are the high Th clusters in the deepest parts of the system, separated by a trough or saddle of lower Th values, leading to low Th in the depth range of 500 to 325 m; in terms of salinity, a cluster of high Th corresponds to a cluster of higher salinity (>18 wt.%); the trough of lower salinity and temperature supports the model discussed in Section 6 of two, possibly transitional, ore-making events.

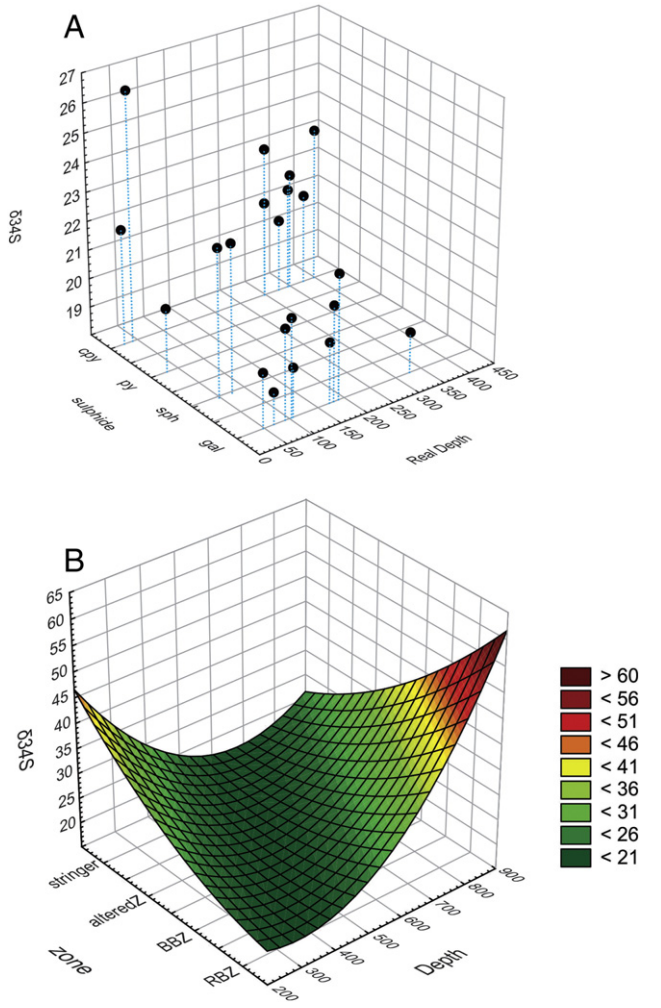

Fig. 17. Sulphur isotope ($\delta^{34}S$) plots for (A) $\delta^{34}S$ values of chalcopyrite, pyrite, sphalerite, galena in relation to actual depth; B); 3D surface plot of $\delta^{34}S$ values in relation to ore zones; data from Austen (2007) and Vogt and Stumpfl (1987) see text for details.

diagram (Fig. 19), with a very high, but imprecise, initial Os ratio of 7.2 ± 4.8 (MSWD = 4.0). The majority of the scatter in the regression is attributable to one data point (187840-A-NM06) which if omitted, yields an isochron age of 1257 ± 53 Ma (initial Os 7.5 ± 2.0, MSWD = 0.81). Details also shown in Appendix 3. This age broadly corresponds to the 1385–1200 Ma Mutherbukin tectonic event in the Gascoyne Complex (Sheppard et al., 2010; Johnson et al., 2011a,b). This event is manifested along a WNW-trending structural corridor of

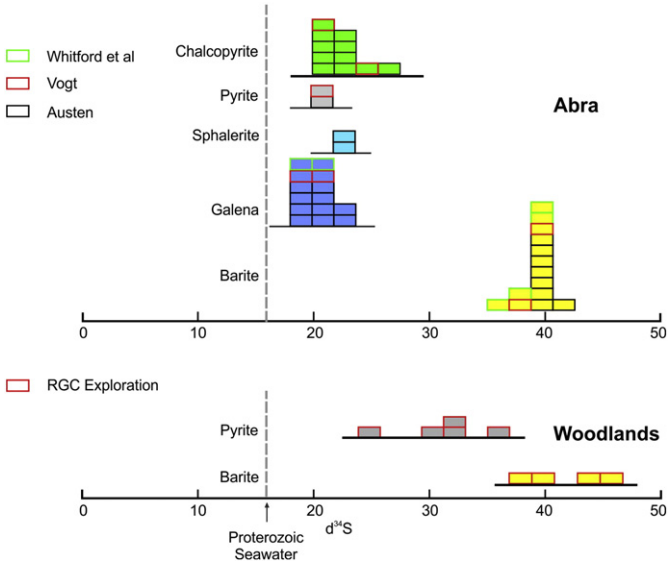

Fig. 16. Histograms of $\delta^{34}S$ values (relative to CDT) for sulphides at Abra and Woodlands (west of Abra, see Fig. 2 for position); note the heavy $\delta^{34}S$ for barites and sulphides in both prospects, probably some of the highest for Proterozoic mineral systems (Faure and Mensing, 2005).

amphibolite facies basement rocks, about 250 km to the northwest of the Abra area. In addition, far-field events that may have resulted in intracratonic reactivation include the Albany-Fraser Orogeny (1345–1260 Ma) and the Musgrave Province (1336–1293 Ma; Mount West orogeny) (Cawood and Korsch, 2008; Smithies et al., 2008). It is possible that the Re–Os age represents a younger re-activation event. Rasmussen et al. (2010) determined an age of ~1385 Ma, based on SHRIMP U–Th–Pb dating, of hydrothermal monazite in sandstone units from the Abra. In addition, these authors also reported a SHRIMP age of xenotime cores from the Tangadee Rhyolite, yielding a possible magmatic age of ~1235 Ma. More recently, hydrothermal xenotime intergrown with hematite–magnetite–galena in the Black Zone yielded an age of ~1594 Ma (Zi et al., 2015). These new 1610–1560 ages for the stratiform Abra mineralisation are consistent with the age of the host Irregully and Kiangi Creek Formations. Cutten et al. (in press) considered that the spread of ages over 50 Ma is interpreted to indicate a prolonged period of hydrothermal alteration which is consistent with the complex relationships between ore minerals in the Black Zone and Red Zone (Pirajno et al., 2010; this work). In addition, Pb model ages of 1640–1580 Ma were reported for galena also from the Black Zone (Collins and McDonald, 1994). Authigenic monazite also from drill core samples records multiple hydrothermal events at ~ 1375, 1221 and 995 Ma, which are coeval with the Mutherbukin Tectonic Event and Edmundian Orogeny (Zi et al., 2015). The pyrite Re–Os date of ~1255 Ma from the Black Zone can therefore be considered as an age of reactivation. This

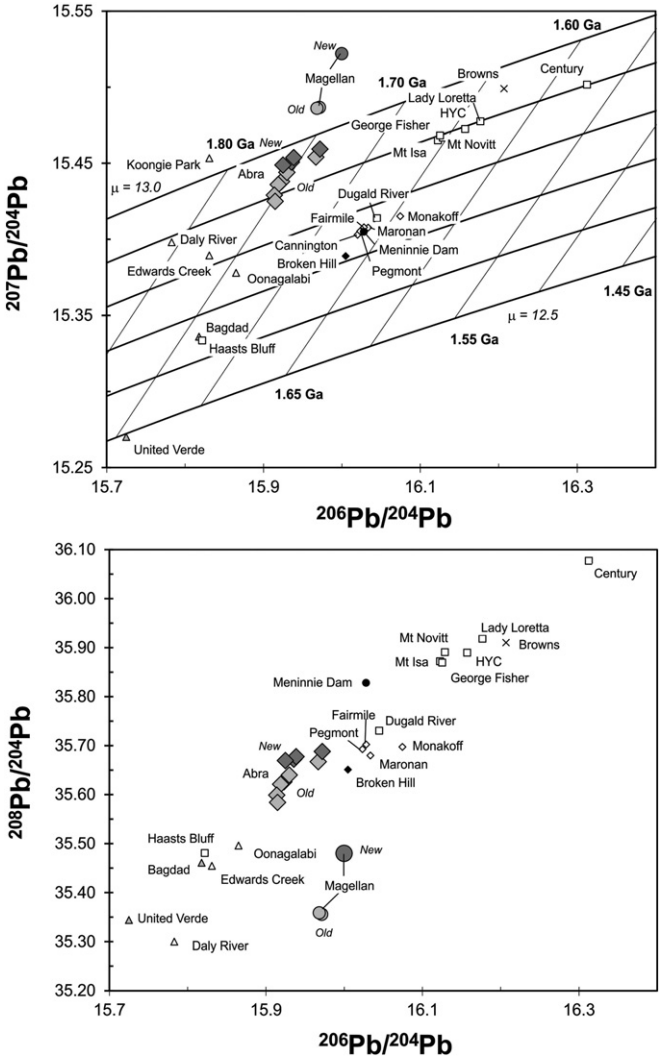

Fig. 18. $^{206}Pb/^{204}Pb$ versus $^{207}Pb/^{204}Pb$ (a) and $^{206}Pb/^{204}Pb$ versus $^{208}Pb/^{204}Pb$ (b) diagrams comparing the Abra lead isotope signature to the least radiogenic signatures of other Proterozoic mineral deposits in Australia and volcanic-hosted massive sulphide deposits in the Yavapai Province of North America (included to show characteristics of lead in more juvenile back-arc settings). With the exceptions previously reported ('old') Abra and Magellan data (Austen, 2007; Pirajno et al., 2010), and data from the Yavapai deposits (Wooden and DeWitt, 1991), Daly River (P Ferenzci, pers. comm., 2005), Koongie Park (Sun et al., 1996) and Browns (McCready et al., 2004), all data are high precision (i.e., double-spike TIMS or ICP-MS) analyses. The high precision data are from Carr et al. (2001), Hussey et al. (2005), Pirajno et al. (2010) and D Huston (unpublished data). For the high precision analyses the analytical uncertainty is similar or smaller than the symbol size (better than 0.03% for each mass ratio).

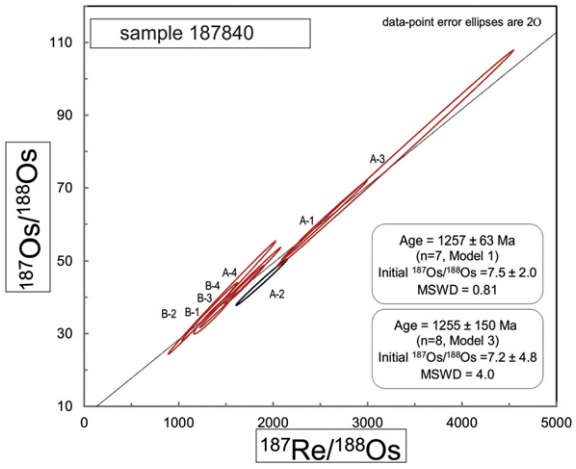

Fig. 19. Re–Os isochron diagram (see also Appendix 4).

is supported by the extremely high initial Os ratio of 7.5 for pyrite, which indicates the common Os incorporated in pyrite had a significant crustal prehistory prior to 1255 Ma at high Re/Os, compatible with derivation from older sulphide minerals.

4. Structural setting of the Abra deposit

The stratigraphy and structure of the Edmund and Collier Basins has been established by many years of 1:100 000 scale geological mapping and detailed research (Martin and Thorne, 2004; Martin et al., 2008), culminating with the recent work reported by Cutten et al. (in press). The Capricorn Seismic Survey (Fig. 3) imaged the deep crustal structure (Johnson et al., 2011a,b, 2012, 2013). The survey extended from the Pilbara Craton in the north across the Capricorn Orogen to the Yilgarn Craton in the south and showed the Paleoproterozoic collisional sutures and reactivated major faults extending to and offsetting the Moho. The Edmund and Collier Basins are well imaged due to the inclusion of dolerites sills which are excellent reflectors. One of the major faults, the Lyons River Fault is the westerly extension of the Quartzite Well Fault which is a very significant structure in Abra mineralisation. An analysis of individual fault movement during deposition of the Edmund Group (Cutten et al., in press) show that the major faults including the Lyons River and Quartzite Well Faults were active, as listric normal faults forming half grabens, since initiation of the Edmund Basin (~1664–1465 Ma). During the post-Edmund Basin Mutherbukin Tectonic Event (1320–1170 Ma) these same faults were reactivated with significant thrust movement in a transpressional environment. During this period extensive structural re-activation may have occurred, perhaps

Table 2
Re–Os isotopic data for pyrite, sample 187840.

Fraction	Re ppb	±2 s	Total Os ppt	±2 s	$^{187}Re/^{188}Os$	±2 s	$^{187}Os/^{188}Os$	±2 s	Rho
A-1	3.194	0.018	54.2	9.9	2542	370	61.10	8.89	0.998
A-2	3.108	0.019	53.7	7.7	1881	223	44.19	5.26	0.995
A-3	2.659	0.021	43.5	17.6	3287	1029	78.02	24.43	0.999
A-4	2.471	0.015	46.6	5.7	1699	172	43.43	4.41	0.993
B-1	1.090	0.012	22.5	4.8	1328	241	36.04	6.54	0.996
B-2	1.161	0.009	22.9	3.4	1373	173	35.53	4.62	0.969
B-3	1.187	0.019	24.3	9.2	1457	465	39.85	12.70	0.998
B-4	1.406	0.014	26.8	6.9	1652	350	42.65	9.04	0.998

ppb = parts per billion.
ppt = parts per trillion.
Rho = error correlation coefficient.

accompanied by seismic activity. As suggested in the seismic profile the Lyons River-Quartzite Well Fault reached into the lithospheric mantle and may have provided a pathway for heated fluids, which generated the mineralising hydrothermal fluids of the Abra deposit. As described by Weatherley and Henley (2013), repeated low magnitude seismic activity is sufficient to build economic mineral deposits in dilational fault jogs, by sudden pressure drop. The recent age determinations of the Abra mineralisation range from 1610 to 1560 Ma, while Re–Os dating of pyrite from the Abra deposit at ~1255 Ma and a Pb–Pb dating of hydrothermal monazite from the host Irregully and Kiangi Creek metasedimentary rocks, at ~1385 Ma, suggest at least two major stages of mineralisation, the first during a period of extensional tectonics that also led to the deposition of the Edmund Group mineralisation and the second during the Mutherbukin Tectonic Event (1320–1170 Ma), perhaps with some later activity during the Edmundian Orogeny (1030–950 Ma).

5. Conceptual models of ore genesis

Vogt and Stumpfl (1987) linked the genesis of the Abra deposit to ~1.64 Ga rift-related tectonics and felsic magmatism. The association of the deposit with felsic magmatism in a rift setting, together with Fe-rich and chlorite alteration of the host sedimentary rocks, raises the possibility that the Abra deposit may be either a variant of the Iberian Pyrite Belt (IPB) mineral systems, which are typically associated with thick siliciclastic successions in a rift setting and exhibit widespread chloritic alteration (Tornos, 2006), or a IOCG-style mineral system, or a SEDEX style mineralisation. However, the IPB deposits have an undeniable link with coeval felsic magmatism and this mitigates in favour of a volcanogenic association. The case is less clear for Abra, although there appears to be a spatial link with felsic volcanism, represented by the Tangadee Rhyolite, which is stratigraphically part of the Kiangi Creek Formation and crops out in the vicinity of the deposit. Nevertheless, the heat energy responsible for the Abra deposit may have been provided by an underlying igneous source together with a mechanism of sulphide precipitation by mixing of S-deficient metalliferous brines with biogenic H_2S-rich fluids. Fluids would have been preferentially exhaled and channelled along the Quartzite Well Fault, along which a range of deposit styles were developed (e.g., breccia pipes, stratiform and/or stratabound metalliferous sediments, vein systems; Abra, Woodlands, Copper Chert, Hyperion, etc. see Fig. 1B). Aeromagnetic images of the area (Fig. 2) support the possibility of the Quartzite Well Fault being the locus of hydrothermal fluids ingress and their lateral migration.

Austen (2007) presented a genetic model, taking into account isotope systematics, fluid inclusions data, oxygen and sulphur isotope thermometry constraints (e.g., sulphide–sulphide and sulphide–sulphate pair). This author noted that the higher temperatures (300–350 °C) are recorded in the Stringer Zone and lower temperatures in the Black Zone (250–325 °C) and Red Zone (200–300 °C). The model invokes metal cations being sourced from a quartz–sandstone aquifer, perhaps with a minor component of Cu from mafic rocks, which may have interacted or mixed with evaporitic brines. The heat source for the flow of the fluids would have been provided by asthenospheric upwelling in the rift basin. Lead and Zn (and Ba) would have been provided by evaporitic brines, whereas Cu, Au, W (and Bi?) would have been brought in by ascending hydrothermal fluids. In the model, bacterial reduction of SO_2 to S_2 or HS^-, was involved in the formation of sulphides. A similar model was introduced by Box et al. (2012) for the Dzhezkazgan and associated sandstone copper deposits of the Chu-Sarysu Basin in Central Kazakhstan.

A tentative genetic model by Pirajno et al. (2010) envisaged that basinal fluids were possibly heated by a deep seated magmatic system, perhaps associated with the Tangadee Rhyolite. Heating of basinal fluids and of pore fluids, could have caused rapid expansion and boiling, resulting in eruption or venting of hydrothermal fluids and the inception of pipe-like structures (Stringer Zone). These eruptions would have occurred time and again, resulting in several stages of hydrothermal activity, as represented by the multiphase hydrofracturing and overprinting textures that are observed in the feeder pipe (Black Zone). The abundance of barite can be explained by leaching of evaporitic minerals in the sedimentary succession. The model suggested that there may be more than one of these hydrothermal breccia pipes and that each of these pipes would be associated with distal hematite–barite chemical sediments, thus enhancing the prospectivity of the Jillawarra Basin.

5.1. A new genetic model

The Abra deposit has features, both in terms of mineral style and tectonic setting (intracontinental rift basin), that are best described as a sedimentary exhalative mineral system (SEDEX).

SEDEX deposits are generally tabular in shape and predominantly contain various amounts of Zn, Pb, Cu, Au, Au, Ag, Ba, Fe and Mn oxides. According to Goodfellow and Lydon (2007) SEDEX architectures range from vent-proximal to vent-distal. The former consists of a vent complex, sulphides Stringer Zone and bedded sulphides, whereas the latter is largerly dominated by bedded deposits. Bedded units, in both cases, comprise hydrothermal products that include chert, barite, carbonates, Fe and Mn oxides and rarely phosphates. In a slightly different model by Leach et al. (2005) (their Fig. 17), an idealised SEDEX has a fault-controlled feeder zone consisting of sulphide vein stockworks, feeding a zone of massive to bedded sulphides, Fe-carbonates, barite and sulphosalts, grading laterally to laminated and/or fragmented sulphides and more distally to chert, barite, hematite, magnetite and Mn oxides. Hydrothermal alteration of the wallrocks, in most instances, include minerals such as quartz, muscovite, chlorite, sericite. In some cases, such as at the Sullivan SEDEX deposit in Canada, post-ore hydrothermal alteration is characterised by albite–chlorite–pyrite in the vent and feeder zones (Goodfellow and Lydon, 2007).

The SEDEX system tends to be sited in the upper parts of continental-derived clastic sedimentary units, such as sandstone, siltstone, mudstone or within intercalated carbonate rocks (Leach et al., 2005; Goodfellow and Lydon, 2007; Pirajno, 2009). SEDEX fluids have a wide range of temperature and salinities. Maximum homogenisation temperatures of approximately 400 °C have been reported from fluid inclusions, but more commonly temperatures ranging from 70 to about 180 °C have been recorded from a number of deposits (Leach et al., 2005; Pirajno, 2009 and references therein). Similarly, maximum salinities of >45% NaCl equivalent are uncommon, with most ranging from about 10 to 23% NaCl. The thermal energy that powers the ore fluids may be the result of high geothermal gradients (e.g., mantle heat in crust attenuated environments), circulation of brines to great depths, or rift-related magmatic activity at depth. The latter is probably the cases for those SEDEX systems that are temporally and spatially associated with intrusive and volcanic rocks. At Abra and surrounding areas there is a lack of significant volumes of intrusive or extrusive rocks, with the exception of the ~1235 Ma Tangadee Rhyolite (Rasmussen et al., 2010), which outcrops a few kilometres to the east of Abra. Sources of ore fluids are mostly basinal metalliferous brines, with the high salinities attributed to dissolution of salts from evaporite beds, although Leach et al. (2005) pointed out that many SEDEX deposits are hosted in sedimentary basins with no evaporites. The metal contents of SEDEX ore fluids is linked to S species in solution, such as H_2S for reduced, acidic with comparatively high temperature fluids (200–300 °C) and SO_4 for oxidised, neutral to alkaline, lower temperature fluids (100–200 °C). Sulphur isotope systematics ($\delta^{34}S$ in SEDEX range generally from −7 to +27‰) indicate that the source of S was likely marine sulphate, followed by bacterial reduction and/or thermochemical reduction of the sulphate (Pirajno, 2009). The upper range of these values compare well with those determined for the Abra sulphides ($\delta^{34}S$ 19 to 26‰).

Fig. 20. Examples of jigsaw (hydrofracturing) in the Stringer Zones from top image Drillhole AB31 (630 m) fragments of chloritic siltstone are cemented by quartz and dolomite with multiple generations of chalcopyrite veinlets (brownish colour); middle and bottom images show close-up views of hydrofracturing in drillhole AB28 (630 m) showing sub-angular to angular quartz cemented by interstitial chlorite and cross-cutting quartz–carbonate veinlets with sulphides and drillhole AB56 (410 m) showing angular to sub-angular fragments of immature volcanic siltstone, or lithic greywacke cemented by chlorite and quartz–carbonate–sulphide material.

Important features of the Abra deposits that need to be considered for a genetic model are: the presence of the stratiform Red Zone (chert and Fe oxides) and associated barites, underlain by rhythmically banded sulphides of the Black Zone, which grades downward into a stringer or stockwork zone. The geometry of the Abra deposit, shown in Fig. 4, and its mineralogical, structural and textural features suggest that the deposit is a SEDEX-style. These features, supported by fluid inclusion studies, isotopic data and petrography, indicate that the Abra mineralisation was the result of at least two principal events: 1) a first stage SEDEX-style system which formed the Red Zone, Black Zone and feeder/Stringer Zone; 2) a later stage characterised by overprinting of the Black and Red Zones by repeated phases of brecciation, ranging from jig-saw type hydrofracturing to fluidisation, examples of which are shown in Figs. 20 and 21. Indeed, the available age data (~1255 Ma by Re–Os on euhedral pyrite, ~1385 Ma on hydrothermal monazite and ~1590 Ma on xenotime from the Black Zone), support a two end-member ore forming stages, although and as highlighted below, the later stage was one of prolonged hydrothermal events associated with movements along the major regional faults, such as the Lyons River and Quartzite Well faults.

The multiple overprinting of the initial SEDEX system is best explained by seismic pressure fluctuations during earthquake activity (e.g., Lindefeld et al., 2012). The general implications for the link between active faults the role of multiphase fluids emission is treated in detail from the structural viewpoint by Micklethwaite et al. (2010). The movement of ore fluids is partly controlled by permeability and enhanced permeability is considered to be proximal to earthquakes, where shear failure is likely to occur, thereby explaining the common fault to shear zone control of ore deposits (Ingebritsen and Appold, 2012). Fault jogs and flower structures are particularly efficient in the channelling of fluids during aftershocks, because these structures promote vertical flow and can tap metal-rich reservoirs (Craw et al., 2013). Importantly, the presence of breccias and veining imply episodic phases of fluid flow and with fluid pressures changing from lithostatic to hydrostatic (Sibson, 1987, 2001; Sibson et al., 1975). Aftershocks, seismic slips and suction-pump mechanisms are induced by rapid transfer of fluids in dilational fault jogs and bends, resulting in the abrupt

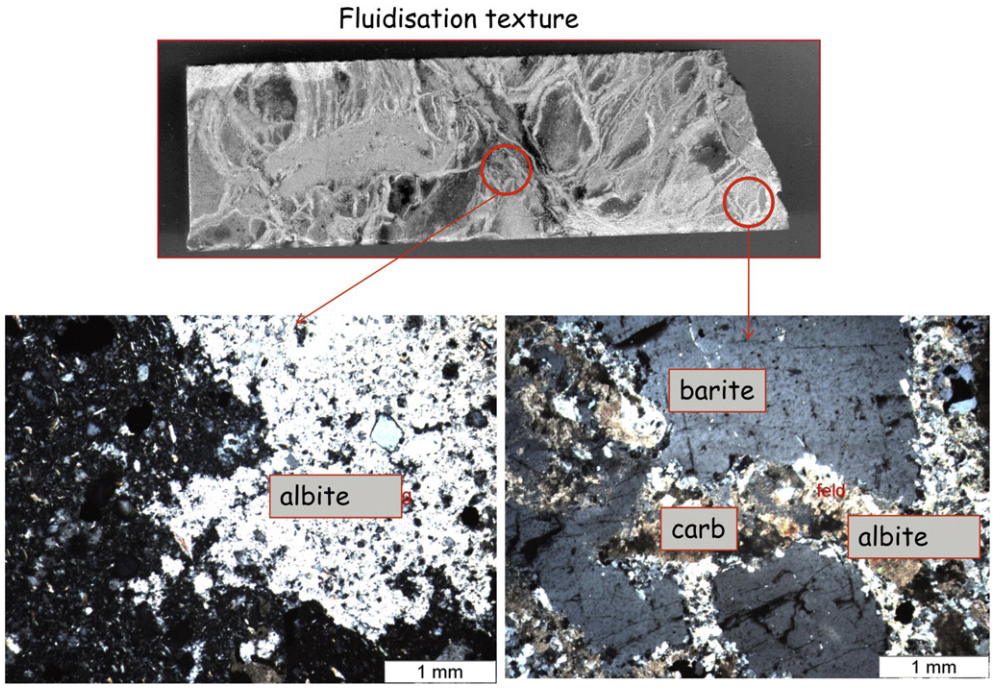

Fig. 21. A fluidised texture from drillhole AB56 (437 m) with large barite crystal overprinted by quartz–feldspar vein, in turn overprinted by carbonate; feldspar (Na or K??; possibly albite) flooding and replacement of siltstone host; locally there is only random nucleation (disseminated) of feldspar in the siltstone matrix; the feldspar is being replaced by carbonate material. Sparsely disseminated pyrite and some galena blebs.

reduction of fluid pressure at structural sites, triggering phase separation and hydrothermal precipitation of ore minerals throughout the aftershock phases (Sibson et al., 1975; Sibson, 2001). These phenomena lead to multiple phases of ore mineral precipitation, accompanied by related alteration minerals. As observed by Craw et al. (2013), there are cases where the precipitation of ores is almost instantaneous and repeated several times during earthquake aftershocks.

We suggest that this may be the case for the Abra breccia pipe, in which hydrofracturing, jigsaw and fluidisation textures are commonly observed and where several phases of ore minerals overprint one another making the construction of a paragenetic sequence very difficult. The protracted seismogenic fault activity may have been responsible for variations of fluid pressures, from lithostatic–supralithostatic (extension and hydraulic fracturing) to hydrostatic–lithostatic regimes resulting in fluid mixing and open space filling. The hydrofracturing is related to gradients in fluid pressure, resulting in a complex and highly dynamic system, in which fracture propagation causes more instability and merging of the hydrofractures, typically with a range of textures from fluidisation to brittle jig-saw style patterns (Figs. 20 and 21).

On the basis of the above discussions, we propose the following idealised (two end-member stages) model, illustrated in Fig. 22a,b. Ore-forming activity resulted from the ingress of hot fluids along a conduit represented by a regional fault and subsidiary structures. The geometry of the Abra deposit would conform with a SEDEX type, exhibiting a feeder zone (epigenetic facies), perhaps with fluids discharging on the sea floor of the time, while clastic sedimentation was still progressing at around 1610–1590 Ma (Fig. 22a). The mineralisation of this stage was typically zoned upward and outward from the point of discharge with proximal syngenetic bedded facies and a distal sedimentary facies as shown in Fig. 22a. The proximal syngenetic facies consisted of rhythmically bedded sulphides (Black Zone), capped by chemical sediments (chert and Fe oxides of the Red Zone), changing laterally to Fe oxides + barite and more distally to Mn-rich chemical sediments. The Manganese Range, between Abra and Woodlands (Fig. 2), may be the result of this lateral and distal chemical sedimentary deposition. In the next stages, between ~1385 and ~1200 Ma, (Fig. 22b) seismic pumping could have been a viable mechanism whereby large quantities of fluids can move along a fault plane during earthquakes to form hydrothermal mineral deposits (Sibson et al., 1975, 1988). The seismic model assumes that just before seismic failure along a strike-slip fault a regime of dilation surrounds the area of the focus. This would be due to increasing shear stress by

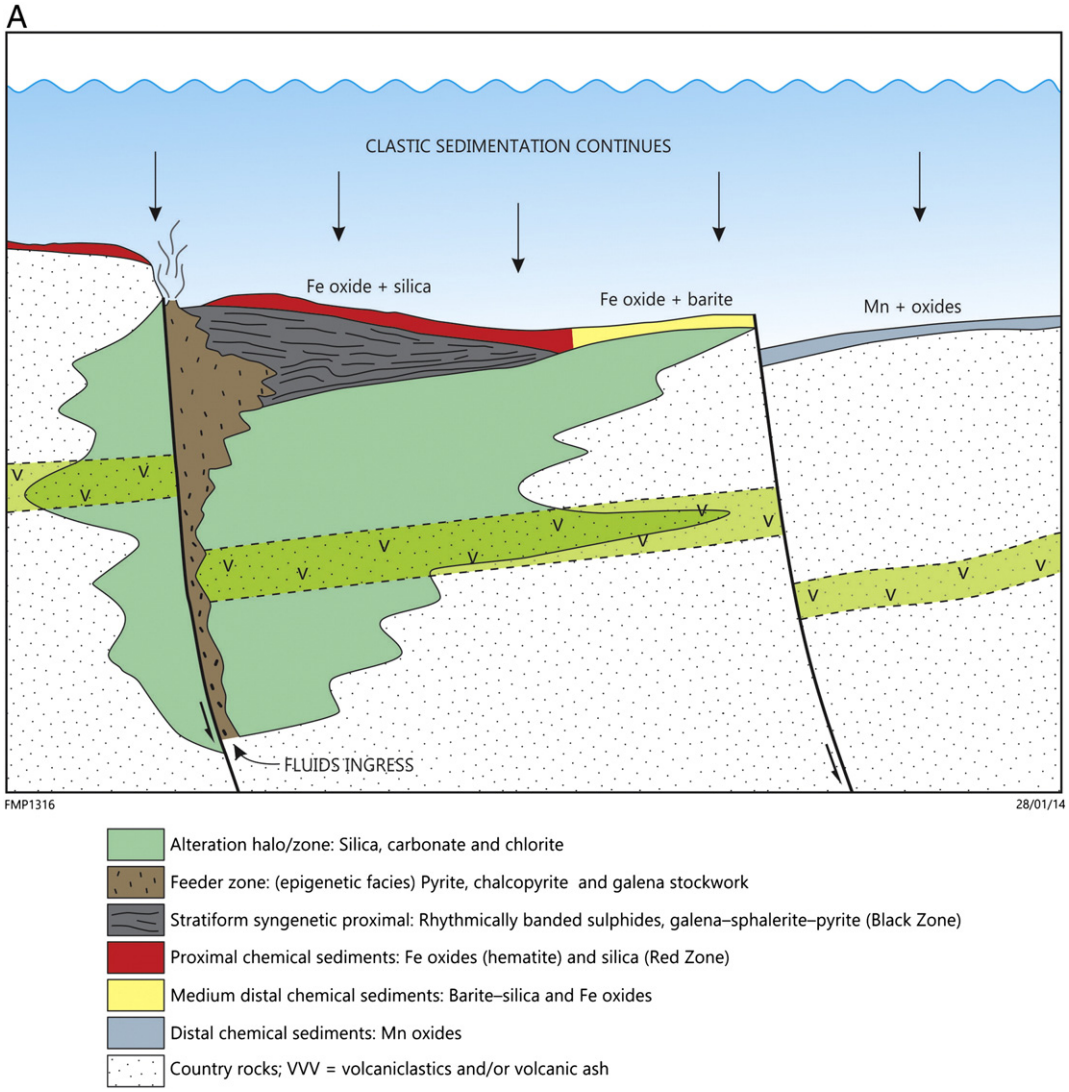

Fig. 22. Idealised ore forming model for the Abra polymetallic deposit; a) SEDEX style stage exhalative system showing an epigenetic facies (feeder pipe, pyrite–chalcopyrite–pyrrhotite) and associated alteration along a conduit, a syngenetic facies of rhythmically banded sulphides (galena–sphalerite–pyrite), capped by banded silica and hematite (oxide bedded facies) and barite; b) renewed fluid flow generating several pulses of hydrothermal activity, enhanced by earthquake, aftershocks and suction-pump mechanisms, resulting in several overprinting phases of the earlier SEDEX style system; the inset at the bottom of the figure shows the seismic pumping model of fluid expulsion along and around an active fault after Sibson et al. (1975).

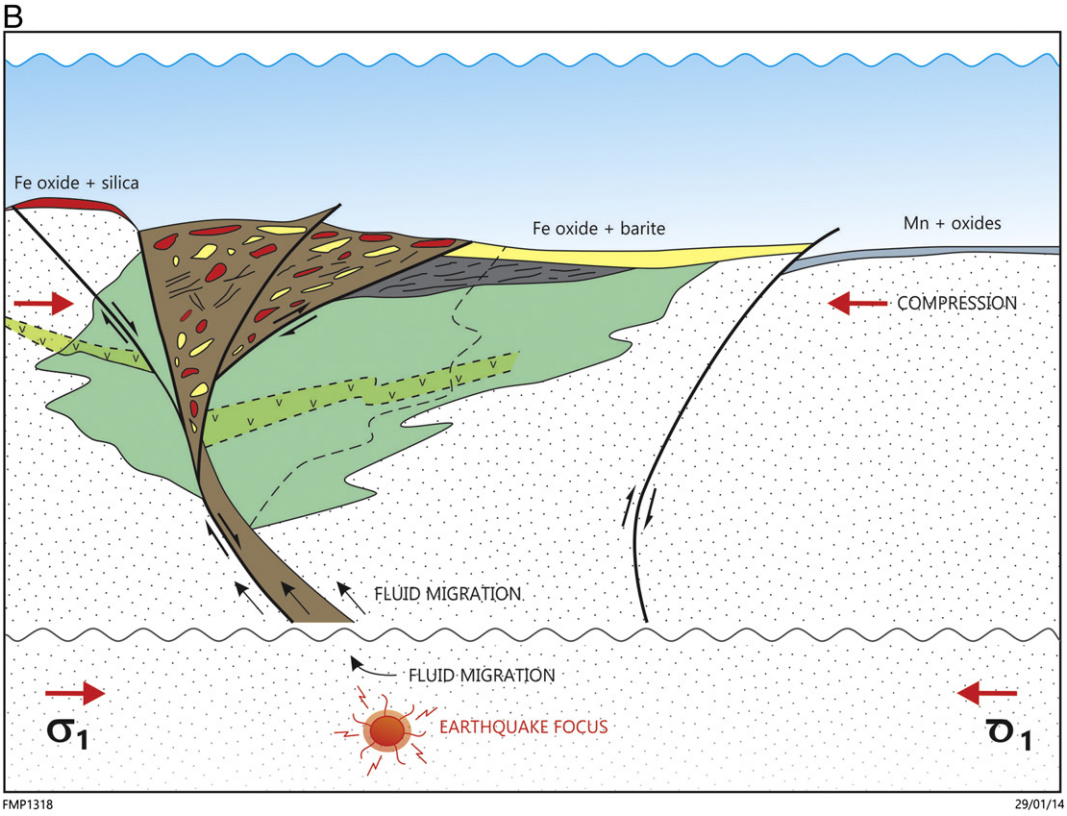

Alteration halo/zone: Silica, carbonate and chlorite
Feeder zone: (epigenetic facies) Pyrite, chalcopyrite and galena stockwork
Stratiform syngenetic proximal: Rhythmically banded sulphides, galena–sphalerite–pyrite (Black Zone)
Proximal chemical sediments: Fe oxides (hematite) and silica (Red Zone)
Medium distal chemical sediments: Barite–silica and Fe oxides
Distal chemical sediments: Mn oxides
Country rocks; VVV volcaniclastics and/or volcanic ash

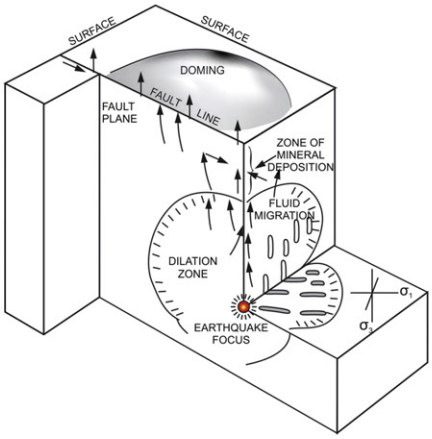

Fig. 22 (*continued*).

the opening of vertical fractures normal to the least principal stress (σ_3), which in the case of strike-slip faults is horizontal. Sibson et al. (1975) argued that the development of these fractures allows the fluid pressure to decrease in the region of dilatancy, resulting in fluid movement along these fractures. Fluid pressure then rises again, accompanied by a decrease in the frictional resistance, so that seismic failure takes place with partial stress relief. The result is the expulsion of the fluids upward in the direction of the pressure relief. This flow of fluids takes place along the fault and nearby fractures, and mineral deposition occurs above the dilation zone. To corroborate their model, Sibson et al. (1975) draw attention to the common observation of hot springs along the active fault. The authors further proposed that if the fault intersects a suitable source region, then metals could be leached out by the moving fluids, transported by seismic pumping and deposited

above the dilatant zone. Sibson et al. (1988) also reiterated that the fault-valve model does provide a suitable account for cyclic fluctuations in fluid pressures from lithostatic to hydrostatic. This quite elegantly explains the range of textures observed in the Abra deposit, from jig-saw fit to fluidised, as exemplified by the occurrence of fragments of Red and Black Zone materials in the lower parts of the Stringer Zone (see core of log of Fig. 5) and the presence of late stage euhedral barite crystals that cut through Fe oxides or fill in open spaces (Figs. 7, 8b, 9d), probably precipitated during phases of pressure release in dilational jogs. Furthermore, bands of late sphalerite and galena cut through the Red Zone (Fig. 5) are likely indicative of late sulphide pulses that overprinted the minerals of the Red Zone. Finally, we draw attention to the 3D diagram of Fig. 15, in which it can be seen that a trough separates two distinctive phases of Th and salinity.

6. Discussion and concluding remarks

For sediment-hosted stratabound mineralisation, Tornos and Heinrich (2008) considered two possible sources of fluids and metals and physico-chemical conditions of material transport: 1) transport of metals and sulphur in different solutions that later mix; 2) transport of metals and sulphate, later reduced in the depositional site. Also there appears to be a genetic relationship between thick siliciclastic successions and giant sulphide deposits, as is the case for the Abra deposit and it may be assumed that the thick sedimentary package of the Edmund Basin may have been the dominant source of the ore metals. The critical feature of SEDEX systems is that the fluids would travel long distances up to a site where the fluid encounters an external source of reduced sulphur, such as a H_2S-rich anoxic basin or a brine pool or a sulphide-rich rock. Barite can only form at very high proportions of seawater and cannot form with massive sulphides in anoxic settings, such as brine pools. Importantly, cooling without mixing with reduced sulphur leads to precipitation of chlorite, chalcopyrite and some pyrite + quartz, but will not produce galena and sphalerite (Tornos and Heinrich, 2008). This explains the enrichment of chalcopyrite in stockworks/Stringer Zones. Most of the Cu in the fluids precipitates by cooling from 350 to 300 °C, utilising the small amount of H_2S in the sediment-equilibrated fluids. Experiments show that for the fluids to reach the low-fS2 (+pyrite + pyrrhotite + arsenopyrite), but chalcopyrite-rich environment of the stockwork/Stringer Zone, requires focused fluid flow under adiabatic conditions (Tornos, 2006; Tornos and Heinrich, 2008).

In the Abra-Woodlands area (Fig. 2), evidence for magmatic fluids is circumstantial, although it is possible that in some of the ore-forming stages magmatism may have provided the heat energy. Stable isotopic signatures suggest derivation of fluids and metals from sedimentary rocks, although magmatic signatures can be masked by isotopic exchange with sedimentary rocks during upflow.

The model that best accounts for the geological, geochemical, isotopic, fluid inclusions and petrographic features of the SEDEX stage of the Abra deposit is flow of basinal brines expelled and circulating from the sedimentary succession of the Irregully Formation. Single-pass dewatering can release enough fluids and leach enough metals to form large orebodies. Mass balance calculations of a sedimentary prism of, say, 100 km by 100 km and 2 km thick, composed of 80% clay and 20% sand, can release somewhere between 7.2×10^{12} to 1×10^{13} m^3 of fluid (Fyfe, 1987, 1994). Single-pass dewatering is a viable process, although fluid flow is ultimately driven by high thermal gradients associated with magmatic systems at depth. Fluid salinities at Abra range from 8 to 22 wt.% NaCl are likely of sedimentary basinal origin, whereas $\delta^{34}S$ values ranging from 19 to 26‰ are indicative of dissolution of evaporites. The Abra SEDEX fluids are probably a mix derived from dewatering of sediments and dissolution of evaporitic minerals. The presence of possible evaporites was mentioned by Vogt and Stumpfl (1987), although these authors did not provide specific evidence. On the other hand, we are reasonably confindent that evaporitic units were present, but are now pervasively silicified.

The identification of evaporite minerals, such as gypsum, anhydrite, or halite, in ancient sedimentary rocks is hampered by their instability during diagenesis and any subsequent metamorphism. They are often replaced initially by other evaporite minerals; these are then in turn replaced by non-evaporite minerals such as calcite, silica, and barite. The result of this diagenetic history is that direct evidence for evaporite minerals in ancient rocks is usually missing and their recognition relies instead on indirect evidence (Warren, 2000). In our case, Abra drill core from a laminated carbonate facies shows wavy, millimetre- to centimetre-scale interlayering of grey microcrystalline dolomite and white microcrystalline ferroan calcite as well as subhedral to euhedral, tabular to rhomboidal, or lenticular clasts of ferroan calcite within a matrix-supported carbonate breccia, which are effectively similar to gypsum pseudomorphs (Alan Thorne, unpublished work and written communication, 2010).

In conclusion, the Abra SEDEX system involved the following:

- Suitable rock package of sediments (siltstone, shale, evaporites)
- High geothermal gradient
- Addition of sulphur by biogenic reduction of sulphates
- Precipitation of sulphides, sulphates, Fe and Mn oxides.

Re-activation events in the Capricorn Orogen that may have influenced the formation of the Abra deposit include the Mangaroon Orogeny (1680–1620 Ma), the Mutherbukin Tectonic Event (1320–1170 Ma), the Edmundian Orogeny (1030–955 Ma) and inversion of the Edmund Basin. The SEDEX part of the Abra deposit may have occurred during the Mangaroon Orogeny, but was later modified by tectonic movements along major faults with recurring seismic tremors, which resulted in the repeated pumping of hydrothermal fluids, which resulted in the multiple overprinting of the Abra SEDEX. Age determinations of individual hydrothermal minerals are continuing and the new data will undoubtedly deliver new light on this unique mineral system.

Acknowledgements

The authors are grateful to the Abra Mining company for allowing the access to drill core and the hospitality at the base camp during several field visits in 2008 and 2009. We also extend our gratitude to Profs Ian Plimer and Chen Yanjing for their insightful reviews, which have considerably improved our paper.

Appendix A. Supplementary data

Supplementary data to this article can be found online at http://dx.doi.org/10.1016/j.oregeorev.2015.04.019.

References

Austen, S., 2007. Isotopic and Thermal Constraints on the Origin and Formation of the Abra Polymetallic Deposit, Jillawara Sub-basin, Western Australia. (Unpublished MSc thesis), School Ocean Sciences, University of Southampton (106 pp.).
Bhattacharyya, D.P., Kakimoto, P.K., 1982. Origin of ferriferous ooids: an SEM study of ironstone ooids and bauxite pisoids. J. Sediment. Petrol. 52 (3), 849–857.
Boddington, T.D.M., 1990. Abra lead–silver–copper–gold deposit. In: Hughes, F.E. (Ed.), Mineral deposits of Australia and Papua New Guinea. Australasian Institute of Mining and Metallurgy, Monograph 14, pp. 659–664.
Box, S.E., Syusyura, Boris, Seltmann, Reimar, Creaser, R.A., Dolgopolova, Alla, Zientek, M.L., 2012. Dzhezkazgan and associated sandstone copper deposits of the Chu-Sarysu Basin, Kazakhstan. In: Michael, Camus, Francisco (Eds.), Geology and genesis of major copper deposits and districts of the world—a tribute to Richard Sillitoe. Society of Economic Geologists Special, Publication 16, pp. 303–328.
Brown, P.E., Hageman, S.G., 1995. Macflincor and its application to fluids in Archaean lode-gold deposits. Geochim. Cosmochim. Acta 59, 3943–3952.
Carpenter, L.C., Garret, D.E., 1959. Tungsten in Searles Lake. Min. Eng. 11, 301–303.
Carr, G.R., Denton, G.J., Korsch, M.J., Parr, J.M., Andrew, A.S., Whitford, D., Wyborn, L.A.I., Sun, S.-S., 2001. User friendly isotope techniques in mineral exploration, Northern

Australian Proterozoic basins. Australian Mineral Industry Research Association Final Report P480 (313 pp.).
Cawood, P.A., Korsch, R.J., 2008. Assembling Australia: Proterozoic building of a continent. Precambrian Res. 166, 1–38.
Cawood, P.A., Tyler, I.M., 2004. Assembling and reactivating the Proterozoic Capricorn Orogen: lithotectonic elements, orogenesis and significance. Precambrian Res. 128, 201–218.
Chi, G.X., Ni, P., 2007. Equations for calculation of NaCl/(NaCl + $CaCl_2$) ratios and salinities from hydrohalite melting and ice melting temperatures in the H_2O–NaCl–$CaCl_2$ system. Acta Petrol. Sin. 23, 33–37.
Collins, P.L.F., McDonald, I.R., 1994. A Proterozoic sediment-hosted polymetallic epithermal deposit at Abra in the Jillawarra sub-basin of the central Bangemall Basin, Western Australia. Proceedings: Geological Society of Australia, 12th Australian Geological Convention, Perth, Western Australia, Abstracts 37, pp. 68–69.
Cooper, R.W., Langford, R.L., Pirajno, F., 1998. Mineral occurrences and exploration potential of the Bangemall Basin. Geological Survey of Western Australia Report 64 (42 pp.).
Craw, D., Upton, P., Horton, T., Williams, J., 2013. Migration of hydrothermal systems in an evolving collisional orogen, New Zealand. Mineral. Deposita 48, 233–248.
Cumming, G.L., Richards, J.R., 1975. Ore lead isotope ratios in a continuously changing earth. Earth Planet. Sci. Lett. 28, 155–171.
Cutten, H.N., Johnson, S.P., Thorne, A.M., Pirajno, F., Wingate, M.T.D., Zwingmann, H., Blay, O., 2015. Structure, deformation and mineral systems of the Edmund and Collier Basins, Capricorn Orogen. Geological Survey of Western Australia Report 127 (in press).
Eldridge, C.S., Bourcier, W.L., Ohmoto, H., Barnes, H.L., 1988. Hydrothermal inoculation and incubation of chalcopyrite disease in sphalerite. Econ. Geol. 83, 972–989.
Faure, G., Mensing, T.M., 2005. Isotopes: Principles and Applications. 3rd edn. John Wiley and Sons, New Jersey.
Fyfe, W.S., 1987. The fluid inventory in the crust and its influence on crustal dynamics. Geol. Assoc. Can. Spec. Pap. 33, 1–3.
Fyfe, W.S., 1994. The water inventory of the Earth: fluids and tectonics. Geological Society, London, Special Publication 78 pp. 1–7.
Goodfellow, W.D., Lydon, J.W., 2007. Sedimentary exhalatove (SEDEX) deposits. Geological Association of Canada, Mineral Deposits Division, Special Publication 5 pp. 163–183.
Hussey, K., Huston, D.L., Claoue-Long, J., 2005. Geology and origin of some Cu–Pb–Zn (Au–Ag) deposits in the Strangways Metamorphic Complex, Arunta Region, Northern Territory. Northern Territory Geological Survey Report 17 (96 pp.).
Ingebritsen, S.E., Appold, M.S., 2012. The physical hydrogeology of ore deposits. Econ. Geol. 107, 559–584.
Johnson, S.P., Sheppard, S., Rasmussen, B., Wingate, M.T.D., Kirkland, C.L., Muhling, J.R., Fletcher, I.R., Belousova, E.A., 2011a. Two collisions, two sutures: punctuated pre-1950 Ma assembly of the West Australian Craton during the Ophthalmian and Glenburgh Orogenies. Precambrian Res. 189 (3–4), 239–262.
Johnson, S.P., Sheppard, S., Thorne, A.M., Rasmussen, B., Fletcher, I.R., Wingate, M.T.D., Cutten, H.N., 2011b. The role of the 1280–1250 Ma Mutherbukin Tectonic Event in shaping the crustal architecture and mineralization history of the Capricorn Orogen. Geological Survey of Western Australia 2011 extended abstracts: promoting the prospectivity of Western Australia. Geological Survey of Western Australia, Record 2011/2, pp. 1–3.
Johnson, S.P., Thorne, A.M., Cutten, H.N., Blay, O.A., 2012. Geological interpretation of the western Capricorn Orogen in Capricorn Orogen seismic and magnetotelluric (MT). Workshop 2011, extended abstracts. In: Johnson, S.P., Thorne, A.M., Tyler, I.M. (Eds.), Geological Survey of Western Australia, Record 2011/25.
Johnson, S.P., Thorne, A.M., Tyler, I.M., Korsch, R.J., Kennet, B.L.N., Cutten, H.N., Goodwin, J., Blay, O.A., Blewett, R.S., Joly, A., Dentith, M.C., Aitken, A.R.A., Holzschuh, J., Salmon, M., Reading, A., Heinson, G., Boren, G., Ross, J., Costello, R.D., Fomin, T., 2013. Crustal architecture of the Capricorn Orogen, Western Australia and associated metallogeny. Aust. J. Earth Sci. 60, 681–705.
Kwak, T.A.P., 1987. W-Sn Skarn Deposits. Elsevier, Amsterdam (439 pp.).
Leach, D.L., Sangster, D.F., Kelley, K.D., Large, R.R., Garven, G., Allen, C.R., Gutzmer, J., Walters, S., 2005. Sediment-hosted lead-zinc deposits: a global perspective. Econ Geol 100th Anniversary Issue pp. 561–607.
Lindefeld, M., Rümpker, G., Link, K., Koehn, D., Batte, A., 2012. Fluid-triggered earthquake swarms in the Rwenzori region, East African Rift—evidence for rift initiation. Tectonophysics 566–567, 95–104.
Lyons, T.W., Gellatly, A.M., McGoldrick, P.J., Kah, L.C., 2006. Proterozoic sedimentary exhalative (SEDEX) deposits and links to evolving global ocean chemistry. In: Kesler, S.E., Ohmoto, H. (Eds.), Evolution of Early Earth's Atmosphere, Hydrosphere, and Biosphere—Constraints from Ore Deposits. Geological Society of America Memoir 198, pp. 169–184.
Martin, D.M., 2003. Peperite in the Backdoor Formation and its significance to the age and tectonic evolution of the Bangemall Supergroup. Geological Survey of Western Australia Annual Review 2002–03, Perth, Western Australia pp. 53–59.
Martin, D. McB, Thorne, A.M., 2004. Tectonic setting and basin evolution of the Bangemall Supergroup in the northwestern Capricorn Orogen. Precambrian Res. 128, 385–409.
Martin, D.M., Sircombe, K.N., Thorne, A.M., Cawood, P.A., Nemchin, A.A., 2008. Provenance history of the Bangemall Supergroup and implications for the Mesoproterozoic paleogeography of the West Australian Craton. Precambrian Res. 166 (1–4), 93–110.
McClung, C.R., Gutzmer, J., Beukes, N.J., Mezger, K., Strauss, H., Gertloff, E., 2007. Geochemistry of bedded barite of the Mesoproterozoic Aggeneys-Gamsberg Broken Hill-type district, South Africa. Mineral. Deposita 42, 537–549.
McCready, A.J., Stumpfl, E.F., Lally, J.H., Gee, R.D., 2004. Polymetallic mineralization at the Browns Deposit, Rum Jungle Mineral Field, Northern Territory, Australia. Econ. Geol. 99, 257–277.
Micklethwaite, S., Sheldon, H.A., Bakre, T., 2010. Active fault and shear processes and their implications for mineral deposit formation and discovery. J. Struct. Geol. 32, 151–165.
Morelli, R.M., Bell, C.C., Creaser, R.A., Simonetti, A., 2010. Constraints on the genesis of gold mineralization at the Homestake Gold Deposit, Black Hills, South Dakota, from rhenium–osmium sulfide geochronology. Mineral. Deposita 45, 461–480.
Morris, P.A., Pirajno, F., 2005. Mesoproterozoic sill complexes in the Bangemall Supergroup, Western Australia, geology, geochemistry and mineralization potential. Geological Survey of Western Australia Report 99 (75 pp.).
Nelson, D.R., 1995. Compilation of SHRIMP U–Pb zircon geochronology data, 1994. Geological Survey of Western Australia, Record 1995/3 (244 pp.).
Pirajno, F., 2009. Hydrothermal Processes and Mineral Systems. Springer, Berlin (1250 pp.).
Pirajno, F., Thorne, A., Mernagh, T.P., Creaser, R.A., Hell, A., Cutten, H., 2010. The Abra deposit: a polymetallic mineral system in the Edmund Basin, Capricorn Orogen, Western Australia. Abstracts Volume, IAGOD Symposium, Adelaide 2010 pp. 112–114.
Plimer, I.R., 1994. Stratabound scheelite in metaevaporite, Broken Hill, Australia. Econ. Geol. 89, 423–437.
Plimer, I.R., 2006. Manganoan garnet rocks associated with the Broken Hill Pb–Zn–Ag orebody, Australia. Mineral. Petrol. 88, 443–478.
Rasmussen, B., Fletcher, I.R., Muhling, J.R., Gregory, C., Thorne, A.M., Cutten, H.N., Pirajno, F., Hell, A., 2010. In situ U–Pb monazite and xenotime geochronology of the Abra polymetallic deposit and associated sedimentary and volcanic rocks, Bangemall Supergroup, Western Australia. Geological Survey of Western Australia Record 2010/12 (31 pp.).
Sheppard, S., Rasmussen, B., Muhling, J.R., Farrell, T.R., Fletcher, I.R., 2007. Grenvillian-aged orogenesis in the Palaeoproterozoic Gascoyne Complex, Western Australia: 1030–950 Ma reworking of the Proterozoic Capricorn Orogen. J. Metamorph. Geol. 25, 477–494.
Sheppard, S., Johnson, S.P., Wingate, M.T.D., Kirkland, C.L., Pirajno, F., 2010. Explanatory Notes for the Gascoyne Province. Geological Survey of Western Australia Report.
Sheppard, S., Bodorkos, S., Johnson, S.P., Wingate, M.T.D., Kirkland, C.L., 2011. The Paleoproterozoic Capricorn Orogeny: intracontinental reworking not continent–continent collision. Geological Survey of Western Australia, Report 108 (33 pp.).
Sibson, R.H., 1987. Earthquake rupturing as a hydrothermal mineralizing agent. Geology 15, 704–707.
Sibson, R.H., 2001. Seismogenic framework for hydrothermal transport and ore deposition. Rev. Econ. Geol. 14, 25–50.
Sibson, R.H., Moore, J.M., Rankin, A.H., 1975. Seismic pumping: a hydrothermal fluid flow transport mechanism. J. Geol. Soc. Lond. 131, 653–659.
Sibson, R.H., Robert, F., Poulsen, H., 1988. High angle reverse faults, fluid pressure gold quartz deposits. Geology 16, 551–555.
Smithies, R.H., Howard, H.M., Evins, P.M., Kirkland, C.L., Bodorkos, S., Wingate, M.T.D., 2008. West Musgrave Complex—new geological insights from recent mapping, geochronology, and geochemical studies. Geological Survey of Western Australia record 2008/19 (20 pp.).
Sturesson, U., Heikoop, J.M., Risk, M.J., 2000. Modern and Palaeozoic iron ooids—a similar volcanic origin. Sediment. Geol. 136, 137–146.
Sun, S.-S., Carr, G.R., Page, R.W., 1996. A continued effort to improve lead-isotope model ages. AGSO Res. Newsl. 24, 19–20.
Thorne, A.M., Cutten, H.N., Hell, A., Pirajno, F., 2009. Kiangi Creek Formation paleogeography and the regional setting of the Abra polymetallic deposit. Geological Survey of Western Australia Record 2009/2 pp. 29–30.
Tornos, F., 2006. Environment of formation and styles of volcanogenic massive sulfides: the Iberian Pyrite Belt. Ore Geol. Rev. 28, 259–307.
Tornos, F., Heinrich, C.A., 2008. Shale basins, sulfur-deficient ore brines and the formation of exhalative base metal deposits. Chem. Geol. 247, 195–207.
Vogt, J.H., 1995. Geology of the Jillawara area, Bangemall Basin, Western Australia. Geological Survey of Western Australia Report 40 (107 pp.).
Vogt, J.H., Stumpfl, E.F., 1987. Abra: a stratabound Pb–Cu–Ba mineralization in the Bangemall basin, Western Australia. Econ. Geol. 82, 805–825.
Warren, J.K., 2000. Evaporites, brines and base metals: low-temperature ore emplacement controlled by evaporite diagenesis. Aust. J. Earth Sci. 47, 179–208.
Weatherley, D.K., Henley, R.W., 2013. Flash vaporization during earthquakes evidenced by gold deposits. Nat. Geosci. 17, 1–5.
Wingate, M.T.D., 2002. Age and paleomagnetism of dolerite sills of the Bangemall Supergroup on the Edmund 1:250000 sheet, Western Australia. Geological Survey of Western Australia, Record 2002/4.
Wingate, M.T.D., Pirajno, F., Morris, P.A., 2004. The Warakurna large igneous province: a new Mesoproterozoic large igneous province in west-central Australia. Geology 32, 105–108.
Wooden, J.L., DeWitt, E., 1991. Pb isotopic evidence for the boundary between the Early Proterozoic Mojave and Central Arizona crustal provinces in western Arizona. Ariz. Geol. Soc. Dig. 19, 27–50.
Zi, J., Rasmussen, B., Muhling, J.R., Fletcher, I.R., Dunkley, D.J., Johnson, S.P., Thorne, A.M., Cutten, H.N., Korhonen, F.J., 2015. In situ U–Pb geochronology of xenotime and monazite from the Abra deposit in the Capricorn Orogen: dating hydrothermal mineralization and fluid events along a long-lived crustal structure. Precambrian Res. 260, 91–112.